Chapter 1

# Construction of High-Precision Adiabatic Calorimeter and Thermodynamic Study on Functional Materials

Zhi Cheng Tan, Quan Shi and Xin Liu

Additional information is available at the end of the chapter

http://dx.doi.org/10.5772/intechopen.76151

**Abstract**

In this chapter, a high-precision fully automated adiabatic calorimeter for heat capacity measurement of condensed materials in the temperature range from 80 to 400 K was described in detail. By using this calorimeter the heat capacity and thermodynamic properties of two kinds of function materials, ionic liquid and nanomaterials, were investigated. The heat capacities of IL [EMIM][TCB] were measured over the temperature range from 78 to 370 K by the high-precision-automated adiabatic calorimeter. Five kinds of nanostructured oxide materials, $Al_2O_3$, $SiO_2$, $TiO_2$, $ZnO_2$, $ZrO_2$, and two kinds of nanocrystalline metals: nickel and copper were investigated from heat capacity measurements. It is found that heat capacity enhancement in nanostructured materials is influenced by many factors, such as density, thermal expansion, sample purity, surface absorption, size effect, and so on.

**Keywords:** calorimetry, adiabatic calorimeter, calibration of calorimetric system, heat capacity, phase transition, thermodynamic properties, function materials

## 1. Introduction

Adiabatic calorimetry is one of the most important research methods in the fields of thermochemistry and thermophysics. Many results can be obtained from this method, such as, molar heat capacities over wide temperature range, standard entropy, standard thermodynamic functions; the temperature, enthalpy, entropy and mechanism of phase transition, and other important information concerned with the structure and energetics of substances, which have very significant guiding role for theoretical research and application development of various new substances or materials. But at present high-precision adiabatic calorimeter is not

available from commercial apparatus in the world. In this chapter, hence, we introduce a high-precision fully automatic adiabatic calorimeter constructed in our themochemistry laboratory, and report the thermodynamic property studies of two types of functional materials: ionic liquid and nanomaterials performed by this adiabatic calorimeter.

## 2. Construction of a fully automated high-precision adiabatic calorimeter used for heat capacity measurements of condensed materials in the range from 80 to 400 K

### 2.1. Introduction

Heat capacity is one of the fundamental thermodynamic properties of materials and is very important in many physical and chemical theoretical research programmes and engineering technology designs. Adiabatic calorimetry is the most reliable technique used to obtain heat capacity and other thermodynamic data of substances [1–9]. Research on adiabatic calorimetry has been conducted in our thermochemistry laboratory since 1960s and several adiabatic calorimetric apparatus have been constructed to obtain measurements over the temperature ranges of (4.2-90) K [10–12], (80-400) K [13–21], (70-580) K [18–19], (300-600 K) [20] and (400-700) K [22]. Traditional adiabatic calorimetric experiments have the disadvantages of complicated experimental procedures and large amounts of experimental data which needs to be treated in order to obtain high-precision heat capacity values. Therefore, we have constructed an adiabatic calorimeter which greatly simplifies experimental procedures (by using modern computerized technology together with control theory) which can be used to obtain measurements in the temperature range of (80-40) K. The design was based on our previously reported automated adiabatic calorimetric apparatuses [17, 19]. This new calorimetric instrument has the advantages of compact data acquisition and process system; advanced intellectual level resulting in the powerful processing ability of the software; better stability of measurement; and a higher reliability of data acquisition. For a long time, low temperature adiabatic calorimetry has been used to: determine the heat capacities of various condensed materials; investigate phase transitions of materials; and determine the standard thermodynamic properties of the materials.

### 2.2. The construction of the adiabatic calorimeter

#### *2.2.1. The adiabatic calorimetric system*

The calorimetric system includes a calorimetric cryostat, a data collection system, an adiabatic condition control system and a high vacuum pumping system. The calorimetric cryostat consists of a sample cell, inner and outer adiabatic shields and a high vacuum can. The data collection system consisted of a multi-channel data acquisition/switch unit (Agilent 34970A) [23] for electric energy collection, a 7 1/2 Digit nanovolt micro-Ohm meter (Agilent 34420A) [24] for acquisition of the temperature of the sample cell and a P4 computer equipped with a matched module and interface card GPIB (IEEE 488).The adiabatic condition control system consisted of a high-precision temperature controller (Lake Shore, Model 340) and two sets of six-junction chromel-copel (Ni-55%, Cu-45%) thermocouple piles that were installed between

the sample cell and the inner adiabatic shield and between the inner and outer adiabatic shield, respectively. The high vacuum pump system consisted of a combined rotational mechanical pump and oil diffusion pump (Edwards, Model NXK 333000). The block diagram of the adiabatic calorimetric system is shown in **Figure 1**.

*2.2.2. Sample cell and adiabatic calorimetric cryostat*

The sample cell (see **Figure 2A**) was made of 0.3 mm thick gold-plated copper, 20 mm long, 20 mm in diameter with inner volume of about 6 $cm^3$. Three sheaths were fixed at the bottom of the cell for inserting the platinum thermometer and thermocouples. Electric heating wires(insulated Karma wire of 0.12 mm in diameter, R = 120 Ω)were coiled on the outer wall of cell A small amount of silicone thermally conductive sealant (type HT916, produced by Shanghai Huitian New Chemical Material Company, Limited) was used to seal the lid to the main body of the cell. On the lid there was a section of copper capillary for pumping out the air in the cell and introducing the helium gas to promote thermal equilibrium inside the cell. The capillary was pinched off and the resultant fracture was soldered by solder to ensure the sealing of the cell.

The adiabatic calorimetric cryostat is shown in **Figure 2B**. Two sets of six-junction chromel-copel thermocouple piles were installed between the sample cell and the inner shield, and between the inner and the outer shield to detect the temperature differences between them. The junctions of the thermocouple piles were inserted in the sheath and fixed on the corresponding surfaces whose temperatures were to be measured. The detected signal of the thermal electromotive force (EMF) created by the temperature differences was fed into the temperature controller which controlled the current through the heating wires on the

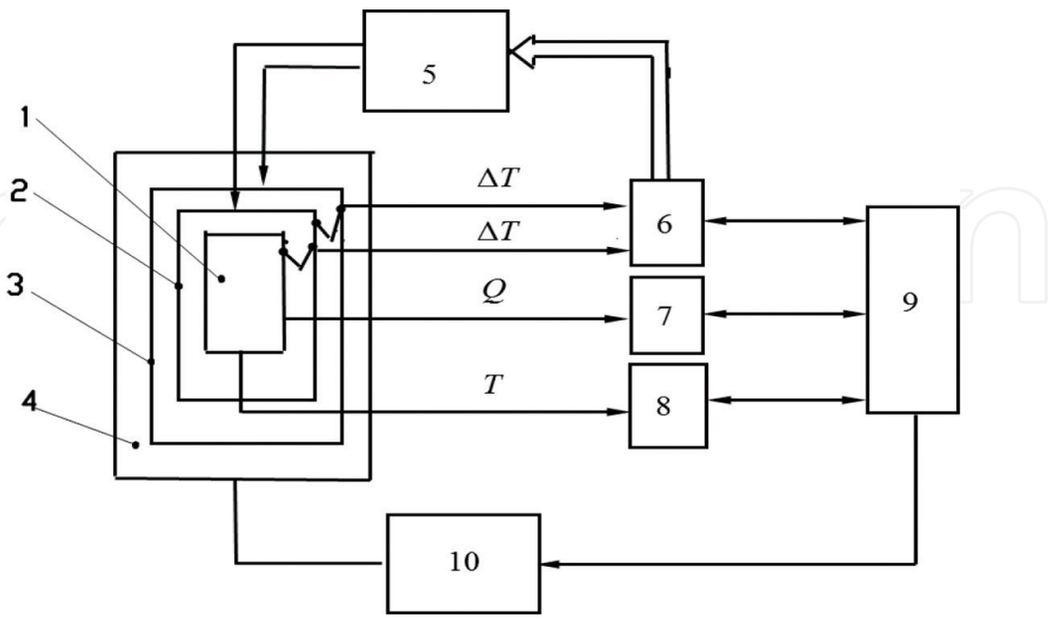


**Figure 1.** Block diagram of the adiabatic calorimetric system. 1, sample cell; 2, inner adiabatic shield; 3, outer adiabatic shield; 4, vacuum can; 5, silicon controlled regulator; 6, temperature controller (Lake shore 340); 7, data acquisition/switch unit (Agilent 34970A); 8, 71/2 digit nanovolt/micro-Ohm meter (Agilent 34420A); 9, computer; 10, combined rotational mechanical pump and oil diffusion pump (Edwards, model—NXK333000).

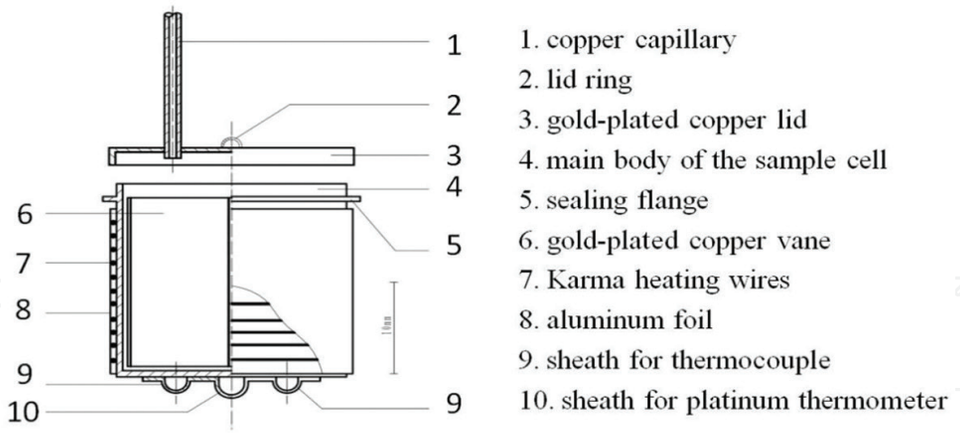


**(A)**

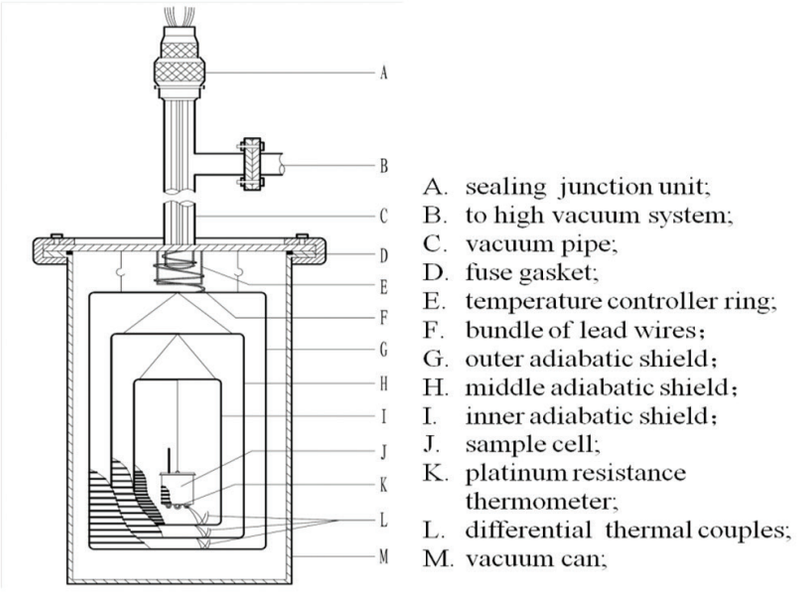


**(B)**

**Figure 2.** (A) Schematic diagram of sample cell of the adiabatic calorimeter. (B) Schematic diagram of main body of the adiabatic calorimeter.

inner and outer adiabatic shields, This heating was used to minimize the temperature difference between the sample cell and the shields thus maintaining a good adiabatic environment.

The sample cell and the adiabatic shields were placed in the high vacuum can to eliminate the heat loss of the cell caused by convection heat transfer. During the heat capacity measurements the vacuum can was evacuated to ($10^{-3}$~$10^{-4}$) Pa by the rotational and diffusion pump.

A precision miniature platinum resistance thermometer (produced by Shanghai Institute of Industrial Automatic Meters, 16 mm long, 1.6 mm in diameter) measured the temperature of the sample cell. The resistance of the thermometer was measured by the 7 1/2 Digit nanovolt/micro-Ohm meter (Agilent 34420A) with four-terminal resistance measurement circuit, and then inputted into the computer for processing after A/D conversion. Then the corresponding temperature was calculated according to the relationship between the resistance

and temperature of the thermometer, which was calibrated in terms of ITS-90 by Station of Low-Temperature Metrology and Measurements, Chinese Academy of Sciences. Here $R_0$ = 100.1384 Ω.

*2.2.3. Computer, data collection unit and software*

The data acquisition system used a P4 computer with Windows Operation System (OS), which had fast computing power and a parallel processing function. The computer collected and controlled data information through GPIB (IEEE 488) card with PCI interface. The interface card (Agilent 82350A) was used in the data exchange because this card has a transmitting speed of 750 $kBs^{-1}$, (here B refers to bytes) which guarantees the information exchanging speed during the experimental process of adiabatic control, collection and control of electrical heating and collection of sample temperatures. The software was programmed to run functions at designated times.

The A/D conversion of all the collected data was done by the data acquisition/switch unit (Agilent 34970A) [23] and 7 1/2 digit nanovolt/micro-Ohm meter, (Agilent 34420A) [24]. The Agilent 34970A had a high precision of data conversion and stability, and had a resolution of 100 nV at 100 mV measuring range, which varies within ±0.0090% over a year. Over the measuring range of our experiments, the resolution of the resistance measurement was 1 mΩ with a variation of ±0.0140%, thus guaranteeing the high precision of data collection. The Agilent 34,420 A nanovolt/ micro-ohm meter was a high-sensitivity multimeter optimized for performing low-level measurements. It combined low-noise voltage measurements with resistance and temperature functions, setting a new standard in low-level flexibility and performance. It has 7 1/2 digits resolution and 100 pV/100 nΩ sensitivity (equivalent to the temperature resolution of $2.5 \times 10^{-5}$ K for the platinum thermometer with $R_0$ = 100 Ω).

The software of the system consisted mainly of three modules (**Figure 3**): data collection and control module, adiabatic environment control module and the module for the setting and revision of the experimental conditions and the data displaying.

The heat capacity measurement was done using an intermittent direct heating method, i.e., loading a certain number of moles (*m*) of sample in the sample cell of the calorimeter followed

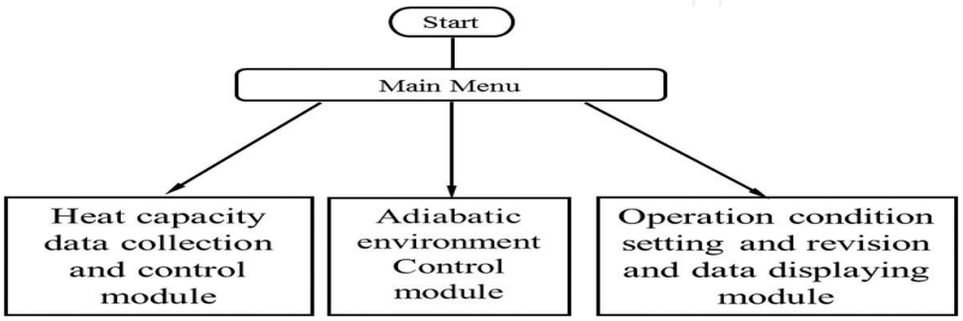


**Figure 3.** The block diagram of the software for calorimetric measurements programmed by computer.

by the input of an appropriate amount of electric energy ($Q$) to induce a temperature rise of the cell ($\Delta T$). From the measured values $Q$ and $\Delta T$ the heat capacity of the sample cell ($C_p$) was determined:

$$C_p = \frac{Q}{m \cdot \Delta T} \tag{1}$$

where

$$Q = IV\tau \tag{2}$$

*and* $I$, $V$ and $\tau$ are current, voltage and duration of heating, respectively.

Accordingly, the heat capacity measurement was made as follows. First the temperature of the sample cell was kept stable under strict adiabatic conditions for a time which is called the temperature equilibrium period. During this period the temperature inside the sample cell was kept in equilibrium by the excellent thermal conductivity of the helium gas which fills the cell and two radial copper vanes fixed to the cell. When the temperature of the sample cell reached equilibrium, the computer system controlled (34970A) the input of an appropriate amount of current $I$ and voltage $V$ used to heat the sample cell to induce a temperature rise of $\Delta T$. The computer system reads the I and V data at intervals (e.g., 30 s) during the heating process. The computer controlled the heating duration and calculated $Q$ from Eq. (2). Following the heating period, the temperature $T$ of sample cell was measured at the next temperature equilibrium period. The temperature increment of the sample cell, $\Delta T$, caused by the energy input was calculated on the basis of the difference in temperatures between the neighboring two equilibrium periods. The heat capacity, $C_p$, was then obtained from Eq. (1). Through repetitions of the above procedures the heat capacity from low temperature to high temperature could be calculated. In order to ensure adequate precision of heat capacity measurements, some problems had to be solved, such as: the determination of the beginning of the equilibrium temperature during the thermal equilibrium period; the precise measurement of the equilibrium temperature of the sample cell; and the temperature correction resulted from the heat exchange between the sample cell and its environment under non-ideal adiabatic conditions.

Following the heating period, the temperature of the sample cell continued to change as a result of the uneven distribution of the temperature of the sample cell caused by the continuous transferring of heat energy and the heat exchange between the sample cell and its environment owing to the non-ideal adiabatic conditions. After some time, however, the temperature variation of the sample cell due to the transferring of heat energy decreased while the heat exchange between the sample cell and its environment continued. Under the condition that the temperatures of the inner and outer shields were keep stable, the heat exchange between the sample cell and its environment become stable and thus there was a linear relationship between the temperature of sample cell and the time of the experimental measurement. According to this principle, the computer fitted several collected temperature points of the sample cell versus time to get the lines $l_i$ or $l_{i+1}$ (see **Figure 4**), whose slope was the variance ratio of the temperature as a function of time. The temperature of the calorimetric system can be regarded as reaching equilibrium if the variance ratio become small enough, e.g., 0.001 K min$^{-1}$, where min refers to minutes.

http://dx.doi.org/10.5772/intechopen.76151

On the other hand, except for the temperature variation, the deviation of the data collection also influences the slope of the line. The effect can be evaluated from the correlation coefficient of the fitted line. The closer the correlation coefficient is to 1, and the more the temperature points are focused around the line, the smaller will be the data collection random error. The present system took the average of the absolute values of the differences between the measured values and the fitted values as the estimation criterion. When the average value was less than some value, e.g., 0.001 K, the random error of the data collection could be neglected.

The collected temperature data were processed automatically by the computer to determine the arrival of temperature equilibrium; when the above two criteria were satisfied the computer deemed that the temperature of the calorimeter had reached equilibrium. Otherwise the temperature measurement time would be prolonged and another temperature point would be collected and the last ten temperature points would be processed with the same method as mentioned above until the two criteria were met.

The precision of the temperature measurement of sample cell correlated with the random error of the temperature data collection. To avoid this kind of error, the system collected a number (e.g., 10) of temperature points after the temperature of sample cell reached equilibrium, ranking them according to the magnitude of the collected values, discarding the maximum and minimum values among them and correcting the error by the figure filter technique:

$$\overline{T} = \frac{1}{K}\sum_{i=1}^{n-2} T_i \tag{3}$$

in which $\overline{T}$ is the corrected temperature value, $K = n-2$, $T_i$ is the collected temperature value, $n$ is the times of the temperature data collection after the temperature equilibrium. The corrected temperatures are shown on $l_i$ and $l_{i+1}$ (see **Figure 4**).

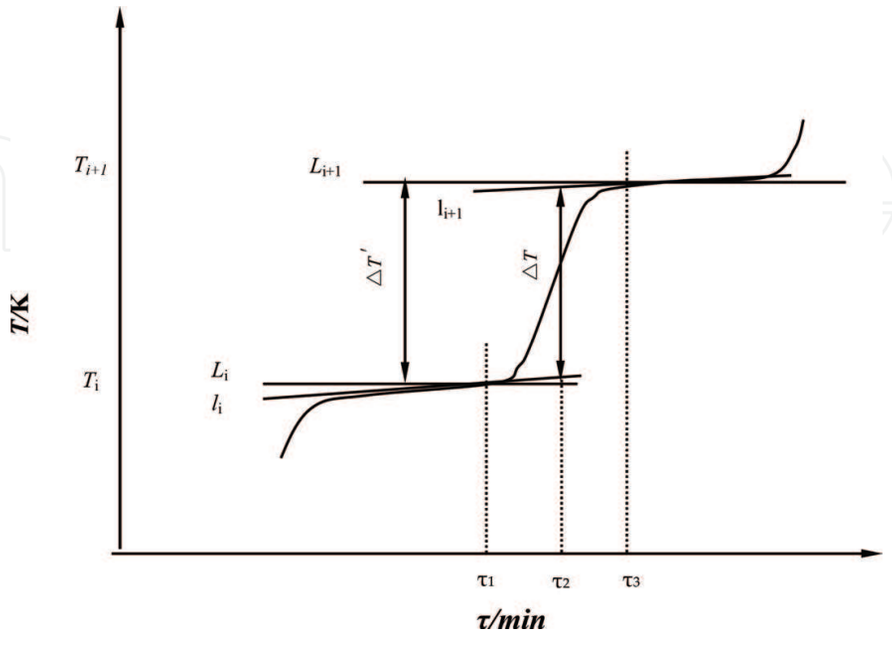


**Figure 4.** The principle diagram of the temperature rise correction.

The temperature rise during the heating period is the result of a combination of the heating of the sample cell by the introduced energy and the heat exchange between the sample cell and its environment caused by the non-ideal adiabatic condition; the latter will lead to some error in the measurement results. In order to correct this error, lines li and li + 1 are extrapolated to intersect with the vertical line of the time axis at the middle point between the beginning and the end of the heating time] (**Figure 4**, $\tau_2 = (\tau_1 + \tau_3)/2$). The distance between the two crossing points is the corrected temperature rise, $\Delta T$, which is just the temperature rise caused by the heat energy introduced during the heating period. This correction is performed through extending lines $l_i$ and $l_{i+1,}$ which are obtained when determining the start of the equilibrium temperature.

Introducing $\Delta T$ into Eq. (1) produces, $C_{p,}$ which is the heat capacity value at the temperature of ($T$i + $T$i$_{+1}$)/2 (see **Figure 4**). The processing procedures are shown in **Figure 5**.

*2.2.4. Adiabatic environment control module*

The premise of good adiabatic conditions is to keep the temperatures of the inner and outer adiabatic shields close to that of the sample cell. In order to do this the heating current introduced into the sample cell is gradually and smoothly increased in the initial period, keeping it at a constant value in the middle period and then decreasing it in the final period. If the temperatures of the inner and outer adiabatic shields are kept increasing synchronously with that of the sample cell, the temperature of sample cell will decrease after the heating period and the speed of the temperature decrease will vary with the species, mass, heat conductivity of the samples and the temperature range of the measurement because of the uneven distribution of the interior temperature of the cell during the heating period. As a result the temperature of the inner shield will become higher than that of the sample cell; this will influence the calculated heat capacity. This system can be considered as an intelligent control of the temperatures of the inner and outer adiabatic shields, that is, it corrects the heating current of the inner adiabatic shield during the latter heating period according to the thermal properties of the sample and the actual condition of the measurement in the corresponding temperature range and controls the temperature of the inner shield at a slightly lower temperature than that of the sample cell to avoid the over regulation of temperature of the inner adiabatic shield, especially for samples with small heat conductivities or samples with phase transitions.

*2.2.5. The module of setting and revision of operation conditions and data displaying*

This system refreshes the screen every time it collects data, displaying in real time the various parameters and states, such as, the electric energy introduced into the sample cell, the temperature of the sample cell, the adiabatic control condition and the environment temperature.

The measuring conditions can be set on the screen before the measurement and revised on the screen during the measurement. At the same time information can be displayed, such as, the heat capacity of the sample which might vary with the temperature and the occurrence of a phase transition, so as to understand the change of thermal properties of the sample at anytime. The parameters and states mentioned above can be displayed on the screen at the same time and can be processed because the software of the system is developed under a multi-file application program with a multi-channel module.

http://dx.doi.org/10.5772/intechopen.76151

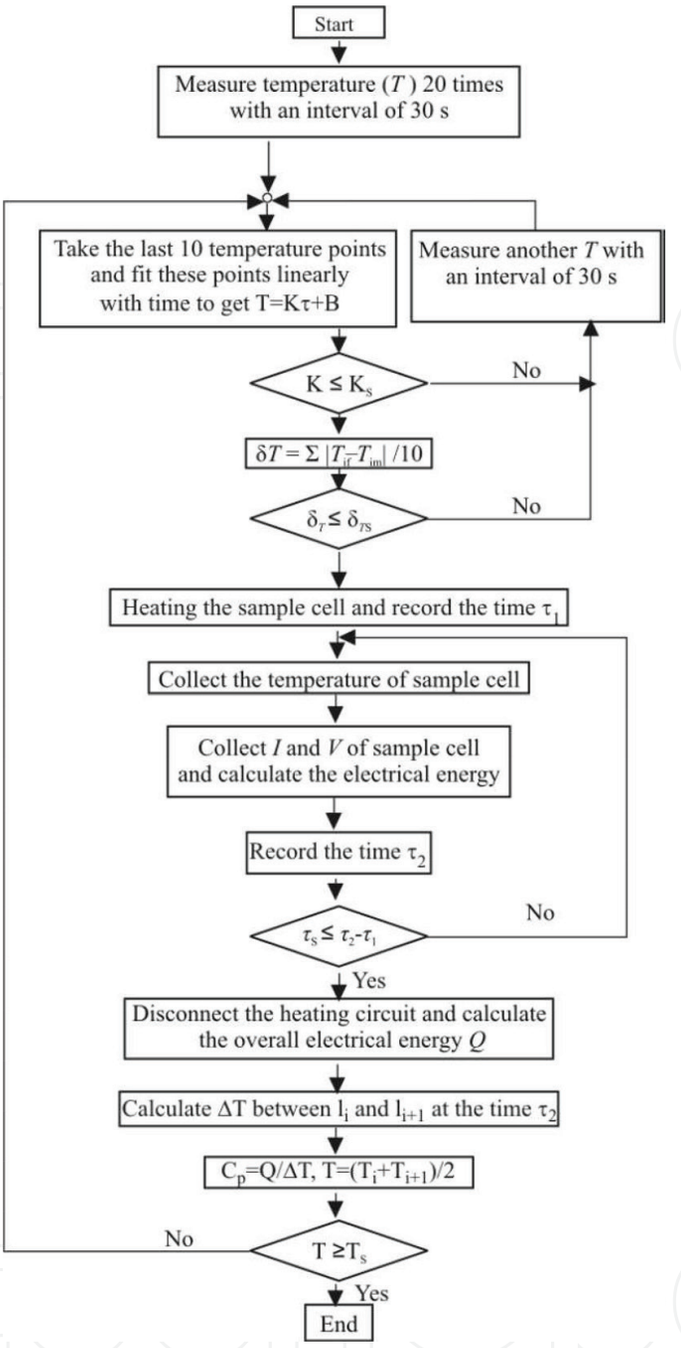


**Figure 5.** Block diagram of acquisition and processing for heat-capacity data controlled by computer.

### 2.3. Calibration of the calorimeter and discussion of results

The reliability of the constructed adiabatic calorimetric system was verified by measuring the molar heat capacities of synthetic sapphire ($\alpha$-$Al_2O_3$, Standard Reference Material 720).The results are listed in **Table 1**. In order to compare the values with those recommended by NIST [25], we calculated the molar heat capacities of $\alpha$-$Al_2O_3$ in the temperature range of (80–400) K at intervals of 10 K using a non-linear insert method based on the measured molar heat capacity data. The results are listed in **Table 2** and shown in **Figure 6**, from which it can be seen that

the deviations of our values from the recommended values are within ± 0.1%, which indicates that the performance of the constructed calorimetric apparatus has been improved compared with previous calorimeters.

Compared with the previous calorimetric system, the newly improved system has the advantages of: compaction; is a simplified device, exhibits great stability and precision; and operates at a higher intellectual level with greater software power than previous reported calorimeters. After operating and testing the equipment for one and a half years we can confirm that the calorimetric system is: easy to operate; performs in a stable manner; and is able to perform

| $T$ (K) | $C_p$ (J K$^{-1}$ mol$^{-1}$) | $T$ (K) | $C_p$ (J K$^{-1}$mol$^{-1}$) | $T$ (K) | $C_p$ (J K$^{-1}$mol$^{-1}$) |
|---|---|---|---|---|---|
| 78.636 | 6.377 | 159.716 | 35.898 | 280.221 | 74.988 |
| 79.621 | 6.725 | 163.370 | 37.371 | 283.636 | 76.003 |
| 80.914 | 7.105 | 166.940 | 38.836 | 286.970 | 76.623 |
| 82.612 | 7.649 | 170.434 | 40.202 | 289.848 | 77.225 |
| 84.261 | 8.043 | 173.857 | 41.462 | 292.652 | 78.015 |
| 85.868 | 8.526 | 177.215 | 42.745 | 295.379 | 78.494 |
| 87.435 | 9.002 | 180.512 | 43.985 | 298.106 | 79.019 |
| 88.968 | 9.467 | 183.752 | 45.191 | 301.288 | 79.646 |
| 90.466 | 9.920 | 186.939 | 46.442 | 304.545 | 80.502 |
| 91.933 | 10.366 | 190.075 | 47.587 | 307.229 | 80.953 |
| 93.370 | 10.812 | 193.163 | 48.720 | 309.918 | 81.498 |
| 94.780 | 11.264 | 196.591 | 49.964 | 312.585 | 82.032 |
| 96.163 | 11.722 | 200.349 | 51.294 | 315.238 | 82.527 |
| 97.522 | 12.178 | 204.043 | 52.561 | 317.878 | 83.033 |
| 98.858 | 12.627 | 207.679 | 53.872 | 320.502 | 83.476 |
| 100.171 | 13.065 | 211.258 | 55.055 | 323.493 | 84.108 |
| 101.464 | 13.501 | 214.781 | 56.284 | 326.855 | 84.726 |
| 102.736 | 13.952 | 221.677 | 58.482 | 330.201 | 85.325 |
| 103.990 | 14.438 | 225.053 | 59.618 | 333.529 | 86.152 |
| 106.588 | 15.363 | 228.384 | 60.716 | 336.818 | 86.670 |
| 110.464 | 16.756 | 231.671 | 61.722 | 340.706 | 87.329 |
| 114.184 | 18.093 | 234.923 | 62.690 | 345.119 | 88.148 |
| 119.983 | 20.085 | 238.140 | 63.684 | 349.510 | 88.825 |
| 120.933 | 20.668 | 241.288 | 64.568 | 353.864 | 89.563 |
| 123.067 | 21.594 | 244.470 | 65.503 | 358.182 | 90.249 |
| 126.341 | 22.851 | 247.582 | 66.492 | 362.435 | 90.734 |
| 129.520 | 24.083 | 250.679 | 67.275 | 366.655 | 91.608 |

| *T* (K) | $C_p$ (J K$^{-1}$ mol$^{-1}$) | *T* (K) | $C_p$ (J K$^{-1}$mol$^{-1}$) | *T* (K) | $C_p$ (J K$^{-1}$mol$^{-1}$) |
|---|---|---|---|---|---|
| 132.614 | 25.297 | 253.746 | 68.197 | 370.843 | 92.381 |
| 135.628 | 26.489 | 256.786 | 69.051 | 374.999 | 93.160 |
| 138.569 | 27.649 | 259.773 | 69.865 | 378.887 | 93.546 |
| 141.441 | 28.771 | 262.804 | 70.671 | 383.002 | 94.013 |
| 144.251 | 29.854 | 265.768 | 71.443 | 387.425 | 94.611 |
| 147.308 | 31.010 | 268.706 | 72.194 | 391.816 | 95.131 |
| 149.304 | 32.036 | 271.620 | 72.936 | 396.207 | 95.735 |
| 152.497 | 33.269 | 274.509 | 73.667 | 400.363 | 96.183 |
| 155.971 | 34.693 | 277.377 | 74.360 | | |

**Table 1.** Experimental molar heat capacities of$\alpha$-$Al_2O_3$ (M = 101.96 g.Mol$^{-1}$).

| *T* (K) | $C_p$ (Fit) (J K$^{-1}$ mol$^{-1}$) | $C_p$ (NIST) (J K$^{-1}$ mol$^{-1}$) | δ* (%) | *T* (K) | $C_p$ (Fit) (J K$^{-1}$ mol$^{-1}$) | $C_p$ (NIST) (J K$^{-1}$ mol$^{-1}$) | δ* (%) |
|---|---|---|---|---|---|---|---|
| 80 | 6.901 | 6.90 | 0.01 | 250 | 67.08 | 67.06 | 0.03 |
| 90 | 9.678 | 9.67 | 0.08 | 260 | 69.82 | 69.80 | 0.03 |
| 100 | 12.85 | 12.84 | 0.08 | 270 | 72.42 | 72.41 | 0.01 |
| 110 | 16.34 | 16.34 | 0.00 | 280 | 74.87 | 74.88 | −0.01 |
| 120 | 20.07 | 20.07 | 0.00 | 290 | 77.20 | 77.23 | −0.04 |
| 130 | 23.95 | 23.95 | 0.00 | 300 | 79.41 | 79.45 | −0.05 |
| 140 | 27.93 | 27.93 | 0.00 | 310 | 81.51 | 81.56 | −0.06 |
| 150 | 31.95 | 31.94 | 0.03 | 320 | 83.49 | 83.55 | −0.07 |
| 160 | 35.95 | 35.94 | 0.03 | 330 | 85.37 | 85.44 | −0.08 |
| 170 | 39.90 | 39.89 | 0.03 | 340 | 87.16 | 87.23 | −0.08 |
| 180 | 43.75 | 43.74 | 0.02 | 350 | 88.84 | 88.92 | −0.09 |
| 190 | 47.50 | 47.50 | 0.00 | 360 | 90.45 | 90.52 | −0.08 |
| 200 | 51.12 | 51.12 | 0.00 | 370 | 91.97 | 92.04 | −0.08 |
| 210 | 54.61 | 54.61 | 0.00 | 380 | 93.41 | 93.48 | −0.07 |
| 220 | 57.95 | 57.95 | 0.00 | 390 | 94.91 | 94.84 | 0.07 |
| 230 | 61.14 | 61.14 | 0.00 | 400 | 96.18 | 96.14 | 0.04 |
| 240 | 64.18 | 64.17 | 0.02 | | | | |

**Table 2.** Comparison of experimental molar heat capacities of $\alpha$-$Al_2O_3$ with the recommended values by NIST, *δ = 100·($C_p$ (Fit) - $C_p$ (NIST))/$C_p$ (NIST). δ is the deviation of the fit value of the experimental molar heat capacities from the recommended values by NIST.

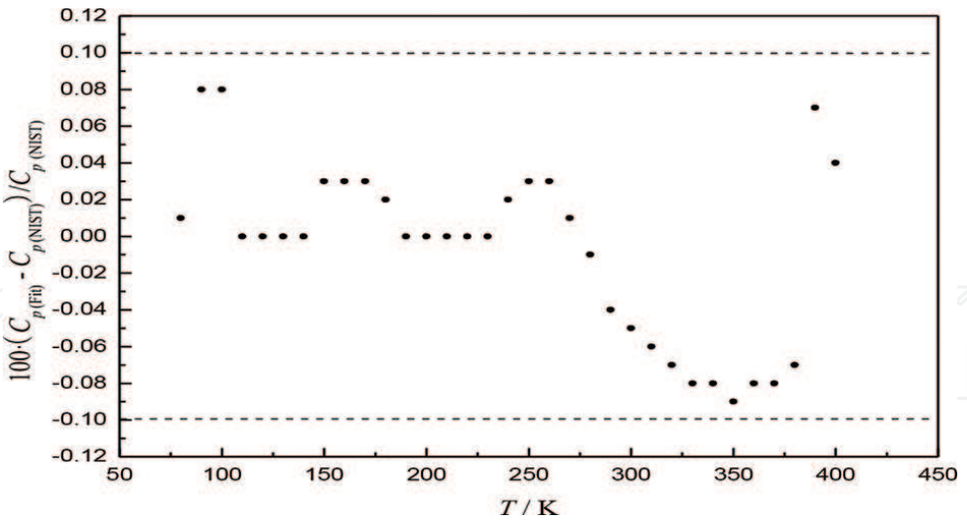


**Figure 6.** Plot of deviations 100·($C_p$ (fit) - $C_p$ (NIST)))/$C_p$ (NIST) of our results for the molar heat capacities of$\alpha$-$Al_2O_3$ from the recommended values by NIST, where $C_p$ (fit) denotes the fit value of our experimental molar heat capacities, $C_p$ (NIST) denotes the recommended values by NIST.

with complete automatic control which includes data processing. All the controlling and measuring procedures can be accomplished through the computer after the sample is loaded in the calorimeter cell. The calorimetric apparatus is now being commercially manufactured.

## 3. Thermodynamic study on functional materials by adiabatic colorimeter

### 3.1. Heat capacity and thermodynamic properties of novel ionic liquid 1-ethyl-3-methylimidazolium tetracyanoborate [EMIM] [TCB]

*3.1.1. Introduction*

During the past decade ionic liquids (ILs) have attracted increasing attention for several reasons. The most striking property is their very low vapor pressure, which suggests their applications as ideal solvents to replace conventional solvents in the frame of "green chemistry." Their highly polar character opens new ways for chemical reactions in homogeneous as well as in biphasic catalyst systems. Special selective solubility for particular components in fluid mixtures give them the potential for use in separation processes. Moreover, properties such as high inherent conductivities, good thermal stability and liquidity over a wide temperature range, opens the way for ILs to be considered as lubricants, thermofluids, plasticizer and electrically conductive liquids in electrochemistry [26] However, the focus by many scientists has been on synthetic, applications in organic chemistry, electrochemistry, and in catalysis, [27–33] while few researchers have worked on the fundamental thermodynamic properties of ILs [26], [34–41] We believe that this has limited the development of using ILs in industry and in the laboratory, and has led us to systematically investigate the thermodynamic properties of ILs.

The novel ionic liquid 1-ethyl-3-methylimidazolium tetracyanoborate ([EMIM] [TCB]) has one of the lowest reported viscosities among ILs. In response to the need for stable hydrophobic ionic liquids, as well as the continuing search for novel materials with technically-relevant properties, Merck KGaA has pursued the development of ionic liquid systems based on the tetracyanoborate (TCB) [42] and tris(pentafluoroethyl)trifluorophosphate (FAP) [43] anions. The resultant IL, [EMIM] [TCB], combines high electrochemical stability with low viscosity; thus providing an ideal ionic liquid for various kinds of electrochemical applications, especially in electrolyte formulations. In addition, its polar nature enables the selective extraction of small polar molecules from aqueous media, like butanol from a fermentation broth.31 Although the novel ionic liquid is very useful in many fields, some of its basic thermodynamic properties are unknown. [34]. As a continuation of our series of research on thermodynamic properties of ionic liquids [34, 38] we have investigated the thermodynamic properties of [EMIM][TCB] including the heat capacity, melting temperature, entropy and enthalpy of fusion, and thermostability by adiabatic calorimetry (AC) and thermogravimetric analytic technique (TG-DTG).

### *3.1.2. Material of the ionic liquid sample and TG analysis*

The ionic liquid, 1-ethyl-3-methylimidazolium tetracyanoborate [$C_{10}H_{11}BN_6$, CAS No. 742099–80-5] was donated by Merck KGaA with labeled purity of 99.9% mass fraction and batch No.S5202031. The clear, colorless, adhesive, liquid sample was transported by an injector and dried under vacuum for 1 day at $T$ = 343 K before the calorimetric measurements were made. The structural formula of the sample is shown in **Figure 7**.

The thermogravimetric (TG) measurements of the sample were carried out by a Thermogravimetric analyzer (Model: Setaram setsys 16/18, SETARAM, France) under high purity argon with a flow rate of 85 ml·min$^{-1}$ at the heating rate of 10 K·min$^{-1}$ from 300 to 1000 K. The sample mass of 45.65 mg was filled into alumina crucible with cover.

From the TG-DTG curve in **Figure 8**, it can be seen that the mass loss of the sample was completed in a single step. The [EMIM][TCB] sample was stable below 570 K. It begins to lose weight at 592.83 K, reaching a maximum rate of weight loss at 677.72 K and completely lost its weight when the temperature reached 791.03 K.

### *3.1.3. Heat capacity measurements*

The heat capacity measurements were carried out in the high-precision automated adiabatic calorimeter mentioned above. The [EMIM] [TCB] sample mass used for the heat capacity measurement was 4.08282 g, which is equivalent to 18.062 mmol based on its molar mass of 226.047 g·mol$^{-1}$.

Experimental molar heat capacities of [EMIM][TCB] measured by the adiabatic calorimeter over the temperature range from 78 to 370 K are listed in **Table 3** and plotted in **Figure 9**. From the Figure, a phase transition was observed at the peak temperature of 283.123 K. According to its reported melting point 286.15 K (MerkK GaA, MSDS) this transition corresponds to a solid–liquid phase change.

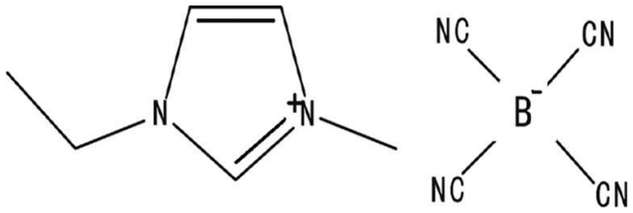


**Figure 7.** Structural formula of 1-ethyl-3-methylimidazolium tetracyanoborate ([EMIM] [TCB]) ionic liquid.

The values of experimental heat capacities were fitted to the following polynomial equations using least square method: [44–45]. For the solid phase over the temperature range 78 to 275 K:

$$C^0_{p,m}/\mathrm{J\cdot K^{-1}\cdot mol^{-1}} = 239.740 + 111.820\,x + 58.242\,x^2 - 65.454\,x^3 - 146.940\,x^4 + 88.43\,3x^5 + 133.050\,x^6 \quad (4)$$

where x is the reduced temperature x = [$T$ – ($T$ max + $T$ min) / 2] / [($T$ max – $T$ min) / 2], $T$ is the experimental temperature, thus, in the solid state (78 to 275 K), x = [($T$ / K) – 176.5] / 98.5, $T$ max is the upper limit (275 K) and $T$ min is the lower limit (78 K) of the above temperature region. The correlation coefficient of the fitting $R^2 = 0.9984$.

For the liquid phase in the temperature range from 285 to 370 K:

$$C^0_{p,m_l}\ \mathrm{J\cdot K^{-1}\cdot mol^{-1}} = 417.200 + 10.749\,x + 6.957\,x^2 - 0.848\,x^3 - 12.377\,x^4 + 0.277\,x^5 + 13.870\,x^6 \quad (5)$$

where x is the reduced temperature, x = [($T$/K) − 327.5]/42.5, $T$ is the experimental temperature, 327.5 was obtained from polynomial $(T_{max} + T_{min})/2$, and the 42.5 was obtained from the polynomial $(T_{max} - T_{min})/2$. $T$max and $T$min are the upper (370 K) and lower (285 K) limit temperature respectively. The correlation coefficient of the fitting $R^2 = 0.9872$.

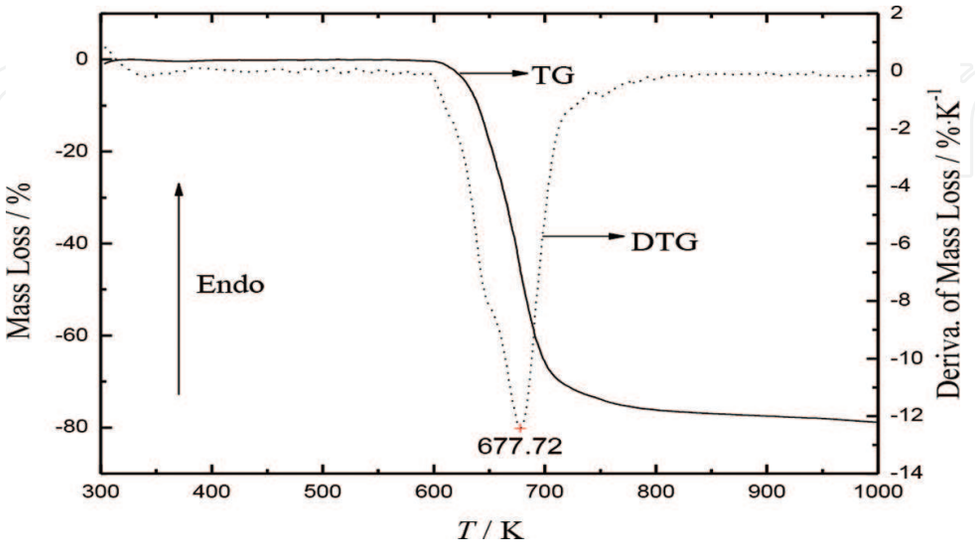


**Figure 8.** TG-DTG curve of [EMIM][TCB] under high purity argon.

| *T* /K | $C_{p,m}^{0}$ /J·K$^{-1}$·mol$^{-111}$ | *T*/K | $C_{p,m}^{0}$ /J·K$^{-1}$·mol$^{-1}$ | *T*/K | $C_{p,m}^{0}$ /J·K$^{-1}$·mol$^{-1}$ |
|---|---|---|---|---|---|
| Series 1 (from 78 to 370 K) | | | | | |
| 77.927 | 146.085 | 177.977 | 241.097 | 277.4682 | 555.844 |
| 79.764 | 148.203 | 179.839 | 243.870 | 279.087 | 767.118 |
| 81.937 | 150.983 | 181.735 | 246.025 | 280.419 | 1202.296 |
| 83.884 | 152.847 | 183.669 | 246.969 | 281.389 | 1903.955 |
| 85.792 | 155.052 | 185.587 | 249.368 | 281.965 | 3018.912 |
| 87.718 | 157.914 | 187.499 | 252.239 | 282.399 | 5399.792 |
| 89.635 | 159.949 | 189.397 | 254.425 | 282.734 | 5575.762 |
| 91.542 | 161.869 | 191.284 | 256.181 | 282.874 | 7564.957 |
| 93.467 | 163.909 | 193.154 | 258.871 | 283.092 | 18761.467 |
| 95.387 | 165.461 | 195.014 | 260.989 | 283.252 | 7044.798 |
| 97.295 | 167.908 | 196.902 | 263.212 | 284.307 | 591.611 |
| 99.207 | 169.054 | 198.825 | 265.888 | 286.576 | 415.399 |
| 101.872 | 171.515 | 200.738 | 268.572 | 287.845 | 411.977 |
| 104.544 | 175.164 | 203.085 | 270.781 | 290.772 | 411.977 |
| 106.458 | 176.259 | 205.410 | 273.551 | 293.390 | 412.401 |
| 108.385 | 178.515 | 207.274 | 275.657 | 295.463 | 412.949 |
| 110.292 | 180.116 | 209.130 | 278.699 | 297.539 | 411.530 |
| 112.211 | 181.765 | 211.039 | 280.437 | 299.615 | 412.321 |
| 114.147 | 183.947 | 213.004 | 282.428 | 301.688 | 412.158 |
| 116.064 | 184.777 | 214.959 | 284.195 | 303.756 | 412.836 |
| 117.953 | 186.418 | 216.904 | 286.319 | 305.827 | 412.703 |
| 119.862 | 189.272 | 218.842 | 288.634 | 307.894 | 412.786 |
| 121.790 | 190.890 | 220.770 | 290.950 | 309.958 | 413.649 |
| 123.696 | 192.142 | 222.689 | 293.965 | 312.022 | 414.143 |
| 125.580 | 194.343 | 224.603 | 296.706 | 314.083 | 414.797 |
| 127.486 | 195.460 | 226.505 | 298.783 | 316.143 | 415.195 |
| 129.403 | 197.570 | 228.393 | 302.507 | 318.200 | 415.380 |
| 131.309 | 199.620 | 230.268 | 305.150 | 320.255 | 415.469 |
| 133.195 | 200.338 | 232.182 | 307.864 | 322.307 | 416.111 |
| 135.096 | 202.129 | 234.157 | 309.324 | 324.357 | 417.116 |
| 137.021 | 203.775 | 236.133 | 311.267 | 326.407 | 416.497 |
| 138.924 | 205.730 | 238.103 | 313.130 | 328.452 | 416.062 |
| 140.817 | 206.818 | 240.060 | 316.506 | 330.493 | 417.738 |

| *T* /K | $C_{p,m}^{0}$ /J·K$^{-1}$·mol$^{-111}$ | *T*/K | $C_{p,m}^{0}$ /J·K$^{-1}$·mol$^{-1}$ | *T*/K | $C_{p,m}^{0}$ /J·K$^{-1}$·mol$^{-1}$ |
|---|---|---|---|---|---|
| 142.689 | 208.471 | 242.369 | 317.531 | 332.537 | 418.451 |
| 144.581 | 211.013 | 244.629 | 319.621 | 334.575 | 418.810 |
| 146.497 | 212.679 | 246.494 | 321.418 | 336.611 | 420.356 |
| 148.391 | 213.957 | 248.351 | 323.883 | 338.648 | 421.073 |
| 150.275 | 215.662 | 250.275 | 327.124 | 340.680 | 422.044 |
| 152.701 | 217.712 | 252.267 | 330.913 | 342.714 | 422.640 |
| 155.148 | 220.702 | 254.246 | 334.647 | 344.743 | 421.688 |
| 157.060 | 221.969 | 256.213 | 337.673 | 346.769 | 422.576 |
| 158.957 | 223.435 | 258.168 | 341.429 | 348.795 | 423.433 |
| 160.842 | 225.899 | 260.113 | 346.133 | 350.823 | 423.405 |
| 162.717 | 225.968 | 262.048 | 351.913 | 352.846 | 424.452 |
| 164.624 | 228.546 | 263.977 | 358.940 | 354.871 | 425.316 |
| 166.570 | 230.426 | 265.896 | 365.659 | 356.888 | 427.998 |
| 168.501 | 232.637 | 267.794 | 376.041 | 358.907 | 427.481 |
| 170.422 | 234.547 | 269.819 | 385.715 | 360.912 | 427.964 |
| 172.328 | 236.398 | 271.924 | 389.540 | 362.920 | 429.779 |
| 174.224 | 238.394 | 273.809 | 428.291 | 364.928 | 429.515 |
| 176.109 | 239.032 | 275.671 | 483.464 | 366.927 | 432.775 |
| Series 2 (from 200 to 350 K) | | | | | |
| 200.914 | 263.743 | 263.694 | 356.567 | 305.827 | 412.703 |
| 204.523 | 267.795 | 264.853 | 357.329 | 309.958 | 413.649 |
| 208.166 | 272.154 | 265.489 | 365.472 | 312.022 | 414.143 |
| 211.126 | 275.978 | 268.275 | 379.717 | 315.143 | 415.195 |
| 214.070 | 279.667 | 271.734 | 389.851 | 318.200 | 415.380 |
| 216.988 | 282.792 | 273.883 | 444.189 | 321.307 | 416.111 |
| 219.952 | 285.992 | 275.895 | 506.737 | 324.357 | 417.116 |
| 222.955 | 289.335 | 277.703 | 618.242 | 327.452 | 418.062 |
| 225.939 | 293.441 | 279.236 | 832.848 | 330.493 | 418.738 |
| 228.900 | 294.685 | 280.434 | 1224.335 | 333.575 | 418.810 |
| 231.807 | 298.703 | 281.294 | 1876.568 | 336.611 | 420.356 |
| 234.776 | 302.820 | 281.897 | 2768.224 | 339.680 | 421.044 |
| 237.799 | 304.937 | 282.310 | 3848.881 | 342.714 | 422.140 |
| 240.796 | 309.951 | 282.603 | 5161.454 | 345.769 | 422.576 |
| 241.316 | 312.567 | 282.820 | 6533.372 | 348.795 | 423.433 |
| 243.839 | 317.567 | 282.982 | 7973.548 | 351.846 | 424.452 |

| *T* /K | $C_{p,m}^0$ /J·K$^{-1}$·mol$^{-111}$ | *T*/K | $C_{p,m}^0$ /J·K$^{-1}$·mol$^{-1}$ | *T*/K | $C_{p,m}^0$ /J·K$^{-1}$·mol$^{-1}$ |
|---|---|---|---|---|---|
| 246.762 | 321.567 | 283.106 | 9917.953 | 354.871 | 425.316 |
| 249.985 | 324.567 | 283.295 | 5149.314 | 357.907 | 426.481 |
| 251.862 | 330.829 | 284.559 | 409.393 | 360.912 | 427.964 |
| 254.943 | 336.749 | 286.799 | 411.977 | 363.928 | 429.015 |
| 257.427 | 339.322 | 290.762 | 411.976 | 366.927 | 432.975 |
| 259.972 | 342.567 | 294.390 | 411.989 | 369.927 | 435.075 |
| 261.233 | 347.567 | 297.539 | 411.530 | | |
| 262.148 | 349.567 | 301.688 | 412.158 | | |
| Series 3 (from 200 to 340 K) | | | | | |
| 198.627 | 222.413 | 249.208 | 255.056 | 288.134 | 347.592 |
| 202.314 | 221.805 | 252.242 | 273.365 | 292.152 | 371.843 |
| 206.065 | 216.489 | 255.264 | 277.024 | 295.213 | 332.434 |
| 209.052 | 224.270 | 258.244 | 268.206 | 298.368 | 419.994 |
| 212.132 | 231.179 | 261.148 | 266.542 | 301.254 | 419.994 |
| 215.313 | 174.192 | 264.050 | 273.986 | 305.664 | 382.918 |
| 217.887 | 199.884 | 266.864 | 294.272 | 309.117 | 265.313 |
| 220.719 | 245.593 | 269.792 | 307.914 | 312.366 | 277.570 |
| 223.749 | 232.252 | 272.608 | 317.557 | 315.485 | 259.491 |
| 226.696 | 240.415 | 275.334 | 390.096 | 318.765 | 223.573 |
| 229.815 | 243.594 | 278.062 | 510.599 | 321.536 | 285.323 |
| 232.774 | 255.469 | 280.873 | 462.126 | 324.117 | 471.394 |
| 235.826 | 269153 | 282.575 | 8988.111 | 328.883 | 200.130 |
| 238.890 | 260902 | 282.990 | 9847.518 | 331.993 | 462.769 |
| 242.563 | 262.842 | 283.172 | 10867.388 | 335.827 | 176.378 |
| 246.192 | 265.801 | 284.767 | 483.962 | | |

**Table 3.** Experimental molar heat capacities of [EMIM][TCB] (M = 226.047 g·Mol$^{-1}$).

### *3.1.4. The temperature, enthalpy and entropy of solid: liquid phase transition*

The standard molar enthalpies and entropies of the solid–liquid phase transition $\Delta_{fus}H_m^0$ and $\Delta_{fus}S_m^0$ of the compound were derived according to the following equations:

$$\Delta_{fus}H_m^0 = \frac{Q - n\int_{T_i}^{T_m} C_{p,m}^0(s)dT - n\int_{T_i}^{T_m} C_{p,m}^0(l)dT - \int_{T_i}^{T_m} H^0(s)dT}{n} \quad (6)$$

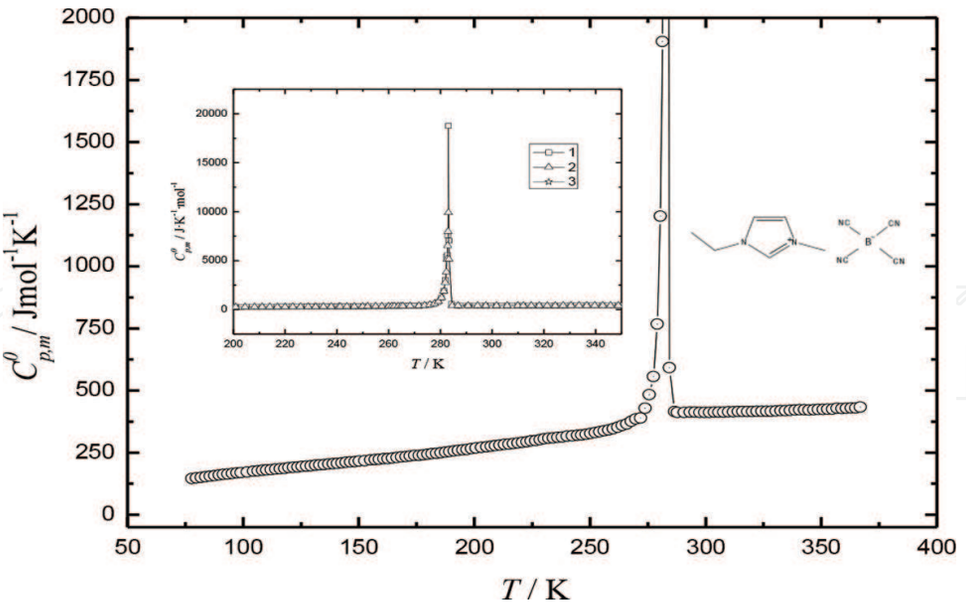


**Figure 9.** Experimental molar heat capacity of [EMIM][TCB] as a function of temperature: outer part from 78 to 370 K for the first series of measurements in the whole temperature range; inner part, from 200 to 350 K of three series of measurements in the melting process.

$$\Delta_{fus} S_m^0 = \frac{\Delta_{fus} H_m^0}{T_m} \tag{7}$$

where $T_i$ is the temperature that is somewhat lower than the temperature of the onset of a solid–liquid transition and Tf is the temperature slightly higher than that of the transition completion. Q the total energy introduced into the sample cell from $T_i$ to $T_f$, $H_0$ the standard heat capacity of the sample cell from $T_i$ to $T_f$, $C^0_{p,m}$(s) the standard heat capacity of the sample in solid phase from $T_i$ to $T_m$, $C^0_{p,m}$(l) the standard heat capacity of the sample in liquid phase from $T_m$ to $T_f$ and $n$ is molar amount of the sample. The heat capacity polynomials mentioned above were used to calculate the smoothed heat capacities, and were numerically integrated to obtain the values of the standard thermodynamic functions above T = 298.15 K. The calculated results of molar enthalpy and entropy of fusion obtained from the three series of heat-capacity were listed in **Table.4**.

### *3.1.5. Thermodynamic functions*

The thermodynamic functions of the [EMIM][TCB] relative to the reference temperature 298.15 K were calculated in the temperature range from 80 to 370 K with an interval of 5 K, using the polynomial equation of heat capacity and thermodynamic relationships as follows:

Before melting,

$$H_T^0 - H_{298.15}^0 = \int_{298.15}^{T} C_{p,m}^0(\mathrm{s})\, d\, T \tag{8}$$

| No | Melting temperature $T_m$ /K | $\Delta_{fus} H_m^0$/ kJ·mol$^{-1}$ | $\Delta_{fus} S_m^0$/J·K$^{-1}$·mol$^{-1}$ |
|---|---|---|---|
| 1 | 283.092 | 12.957 | 45.770 |
| 2 | 283.106 | 12.985 | 45.867 |
| 3 | 283.172 | 12.976 | 45.825 |
| Mean Value | 283.123 ± 0.025 | 12.973 ± 0.008 | 45.821 ± 0.028 |

**Table 4.** The melting temperature, enthalpy and entropy of fusion of [EMIM][TCB] obtained from three series of heat-capacity measurements.

$$S_T^0 - S_{298.15}^0 = \int_{298.15}^{T} \frac{C_{p,m}^0(s)}{T} d\,T \tag{9}$$

After melting,

$$H_T^0 - H_{298.15}^0 = \int_{298.15}^{T_i} C_{p,m}^0(s)\, d\,T + \Delta_{fus} H_m^0 + \int_{T_f}^{T} C_{p,m}^0(l)\, dT \tag{10}$$

$$S_T^0 - S_{298.15}^0 = \int_{298.15}^{T_i} \left[\frac{C_{p,m}^0(s)}{T}\right] dT + \frac{\Delta_{fus} H_m^0}{T_m} + \int_{T_f}^{T} \left[\frac{C_{p,m}^0(l)}{T}\right] dT. \tag{11}$$

where $T_i$ is the temperature at which the solid–liquid phase transition started; $T_f$ is the temperature at which the solid–liquid phase transition ended; $\Delta_{fus} H_m^0$ is the standard molar enthalpy of fusion; $T_m$ is the temperature of solid–liquid phase transition. The standard thermodynamic functions, $[H_T^0 - H_{298.15}^0]$, $[S_T^0 - S_{298.15}^0]$, are listed in **Table 5**.

### 3.2. Heat capacity and thermodynamic properties of nanostructured materials

#### *3.2.1. Introduction*

Nanostructured materials have attracted worldwide attention owing to their special properties. Due to their small grain size and large specific surface, nano materials exhibit many distinctive properties [46]. What are the special thermodynamic properties of nano materials? Can classical thermodynamic theories be used to explain the thermal behavior of nano- materials? These are some of the important questions that must be answered in order to understand the properties of nano- materials more thoroughly and broaden their application areas.

In this chapter we have reported the results of heat capacity measurements of several kinds of nanostructured oxides, metals and zeolites, obtained by low-temperature adiabatic calorimetry, and compared heat capacity enhancement in these materials with the corresponding coarse-grained materials. These data are discussed in the context of properties such as density, thermal expansion, sample purity, surface effect, and size effect. Synthesis of nano materials has been accompanied by adiabatic calorimetry measurements, and materials have been characterized with differential scanning calorimetry (DSC), thermogravimetric (TG) analysis,

| *T*/K | $C_{p,m}^0$/ J·K$^{-1}$·mol$^{-1}$ | $H_T^0 - H_{298.15}^0$/kJ·mol$^{-1}$ | $S_T^0 - S_{298.15}^0$/ J·K$^{-1}$·mol$^{-1}$ |
|---|---|---|---|
| 80 | 150.104 | −70.915 | −360.705 |
| 90 | 158.233 | −69.378 | −342.560 |
| 100 | 169.437 | −67.740 | −325.218 |
| 110 | 180.604 | −65.989 | −308.533 |
| 120 | 190.456 | −64.133 | −292.444 |
| 130 | 198.919 | −62.185 | −276.919 |
| 140 | 206.588 | −60.157 | −261.921 |
| 150 | 214.303 | −58.053 | −247.393 |
| 160 | 222.826 | −55.868 | −233.258 |
| 170 | 232.631 | −53.592 | −219.424 |
| 180 | 243.784 | −51.211 | −205.797 |
| 190 | 255.944 | −48.713 | −192.298 |
| 200 | 268.461 | −46.091 | −178.874 |
| 210 | 280.574 | −43.345 | −165.506 |
| 220 | 291.727 | −40.483 | −152.208 |
| 230 | 301.977 | −37.514 | −139.010 |
| 240 | 312.513 | −34.443 | −125.924 |
| 250 | 326.284 | −31.253 | −112.889 |
| 260 | 348.719 | −27.888 | −99.696 |
| 270 | 388.568 | −24.221 | −85.874 |
| 280 | Melting | | |
| 290 | 412.609 | −5.282 | −18.601 |
| 298.15 | 412.020 | 0.000 | 0.000 |
| 300 | 412.204 | 1.385 | 4.868 |
| 310 | 413.721 | 10.475 | 36.838 |
| 320 | 415.513 | 23.248 | 81.985 |
| 330 | 417.856 | 41.426 | 146.718 |
| 340 | 420.859 | 67.316 | 239.595 |
| 350 | 424.059 | 103.928 | 371.805 |
| 360 | 427.723 | 155.130 | 557.707 |
| 370 | 435.829 | 225.809 | 815.441 |

**Table 5.** Calculated thermodynamic functions of [EMIM][TCB].

thermal expansion coefficient measurements, X-ray diffraction (XRD), transitional electron microscopy (TEM), scanning electron microscopy (SEM), X-ray fluorescence (XRF) and infrared spectroscopy (IR). Full details about the synthesis and characterization of materials were published elsewhere [47].

### *3.2.2. Nanostructured oxides*

Nano oxide materials constitute a rich source of materials. We selected five kinds of oxide materials, $Al_2O_3$, $SiO_2$, $TiO_2$, $ZnO_2$, and $ZrO_2$, which have been widely used, can be prepared by classical methods and obtained with confined size range and high quality.

#### *3.2.2.1. Nano $Al_2O_3$*

We studied molar heat capacity of nano $Al_2O_3$ in the temperature range from 78 to 370 K, and compared with the coarse-grained $Al_2O_3$ [48]. The nanopowder $Al_2O_3$ was processed by hydrolysis of pure aluminum sheet after activation, and the sample purity is more than 99%. The coarse-grained sample of $\alpha$- $Al_2O_3$ is a commercial reagent purchased from Shanghai Chemical Reagent factory with the mass purity of 99.9%. **Figure 10** shows the experimental results indicating that no thermal anomaly took place over the investigated temperature range, but the heat capacities of the nano $Al_2O_3$ was larger than the coarse-grained one and increased with the size decreased. The nano $Al_2O_3$ has excess heat capacity from 6 to 23% as comparing with the coarse-grained one in the temperature range from 200 to 370 K. In the study of infrared spectra, we found that nano $Al_2O_3$ exhibited a blue shift in wave number. This shift indicates that energy structure of nano $Al_2O_3$ is higher than that in coarse-grained state, which is in agreement with the results of heat capacity measurement. To further study the enhancement of heat capacity in nano $Al_2O_3$, we measured the density of nano $Al_2O_3$ to be 89% of the coarse-grained one, and thermal expansion of nano $Al_2O_3$ has been reported to be twice as that of the conventional. All these suggest that the grain boundary of nano materials possesses an excess volume with respect to the perfect crystal lattice, so it seems that the heat capacity enhancement in nano $Al_2O_3$ results from the excess volume.

#### *3.2.2.2. Nano amorphous $SiO_2$*

The molar heat capacity of nano amorphous $SiO_2$ (na-$SiO_2$) was measured over the temperature range from 9 to 354 K. The samples used for experiment were synthesized by using the sol–gel route with hydrolyzing the ethyl tetrasilicate and controlling the chemical reaction conditions. Those samples possess a very high purity (>99.9%). The experimental results were plotted in **Figure 11** together with the molar heat capacity of coarse-grained $SiO_2$ (ca- $SiO_2$). The average grain size of two amorphous $SiO_2$ is also 20 nm and their specific surfaces resulted from BET measurement are 160 $m^2/g$ ($SiO_2$–1) and 640 $m^2/g$ ($SiO_2$–2) respectively. Significant difference in heat capacity between na-$SiO_2$ and ca- $SiO_2$ can be identified from **Figure 11**. The heat capacity enhancement from 150 to 350 K for na- $SiO_2$–1 and na-$SiO_2$–2 are about 2–7% and 4–10% higher than those of ca-$SiO_2$, respectively. The heat capacity values of na-$SiO_2$–2 with larger specific surface are higher about 3% than those of na-$SiO_2$–1. The heat capacity enhancements

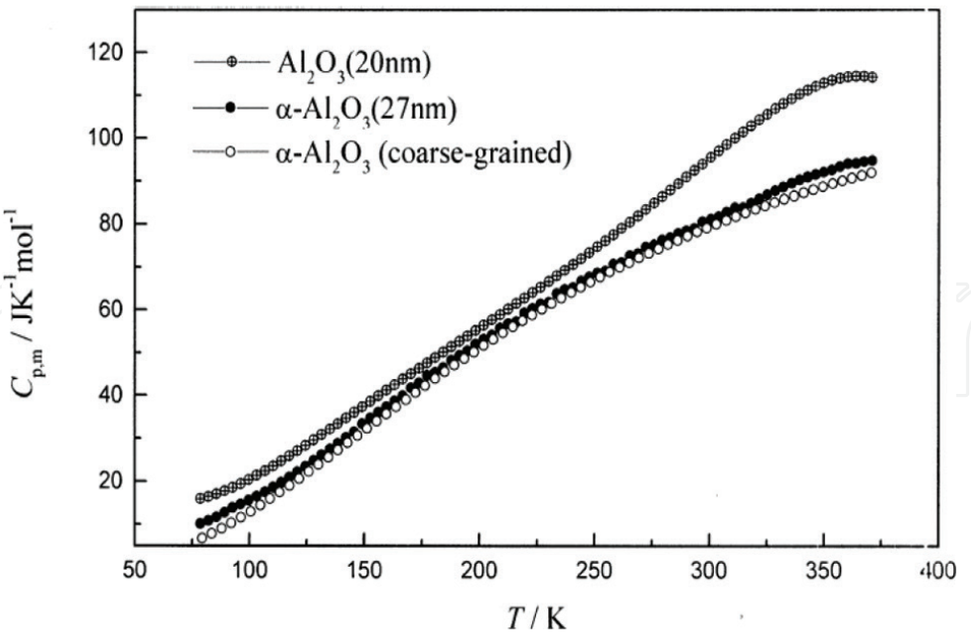


**Figure 10.** Heat capacity of nano and coarse-grained $Al_2O_3$.

in the nanomaterials are usually associated with an increase in the configuration and vibrational entropy of grain boundaries, and the boundaries with larger specific surface will have more configuration and vibrational entropy. So it agrees well with the experimental results that larger grain surface has much contribution to the heat capacity enhancement. We calculated the thermodynamic functions of na-$SiO_2$ based on the heat capacity data. The calculated results were plotted in the **Figure 12**. From the figure, we can conclude that the entropy,

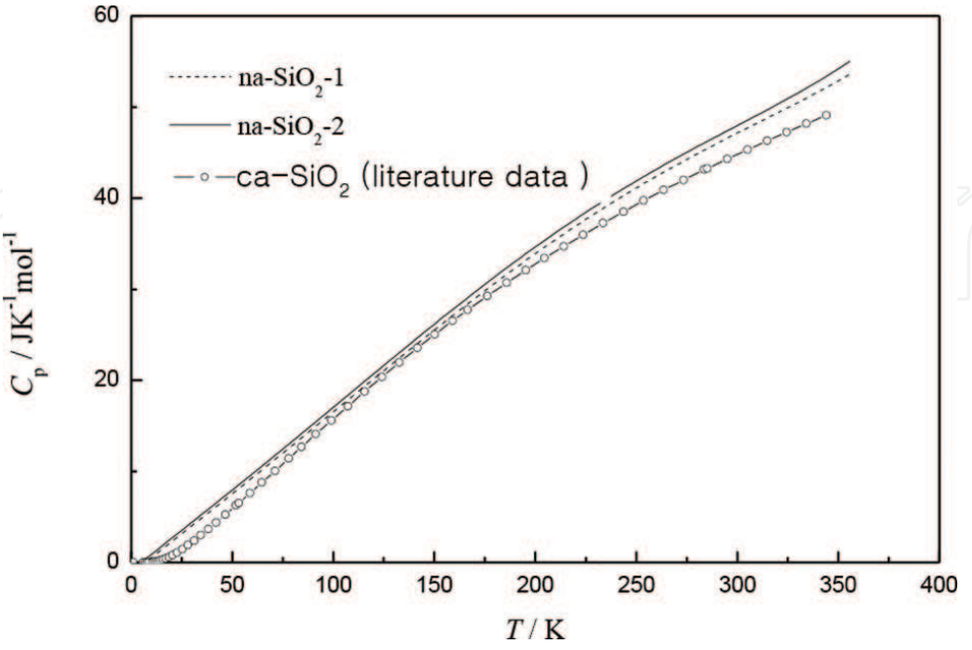


**Figure 11.** Heat capacity of nano amorphous and coarse-grained $SiO_2$ as functions of temperature.

http://dx.doi.org/10.5772/intechopen.76151

enthalpy and Gibbs free energy of larger specific surface na-$SiO_2$ is higher than those of the small one, and the Gibbs free energy is lower, implying larger specific surface materials have complicated disorder, large potential energy and high activity.

*3.2.2.3. Nanocrystalline ZnO*

The two nanocrystalline forms of ZnO studied are ZnO-1 and ZnO-2 with grain size of 65 and 18 nm, respectively. The purity of both two samples is more than 99%. Heat capacity of nanocrystalline ZnO was compared with the literature data [49] of coarse-grained ZnO (c-ZnO) in **Figure 13**. It can be seen that the heat capacities of ZnO-1 is no obviously difference from that of c-ZnO. However, there is large excess heat capacity of 4–17% for ZnO-2 compared with c-ZnO. The similar result was also reported by other researchers. Heat capacity of a material is directly related to its atomic structure, or its vibrational and configurational entropy which is significantly affected by the nearest-neighbor configurations. Nanocrystals are structurally characterized by the ultrafine crystalline grains, and a large fraction of atoms located in the metastable grain boundaries in which the nearest-neighbor configurations are much different from those inside the crystallites. In other words, the grain-boundary possesses an excess volume with respect to the perfect crystal lattice. Therefore, heat capacities of nanocrystals are higher than those of the corresponding coarse-grained polycrystalline counterparts. Although slight impurity can enhance the heat capacity obviously [50], the impurity effect on those two specimens should be very slight. The samples were heated at temperature up to 570 K for 2 h and sample cells were evacuated to be high vacuum ($10^{-5}$ Pa), which can remove the absorbed gas and vapor. So the main contribution of the excess heat capacity of nanocrystaliline ZnO-2

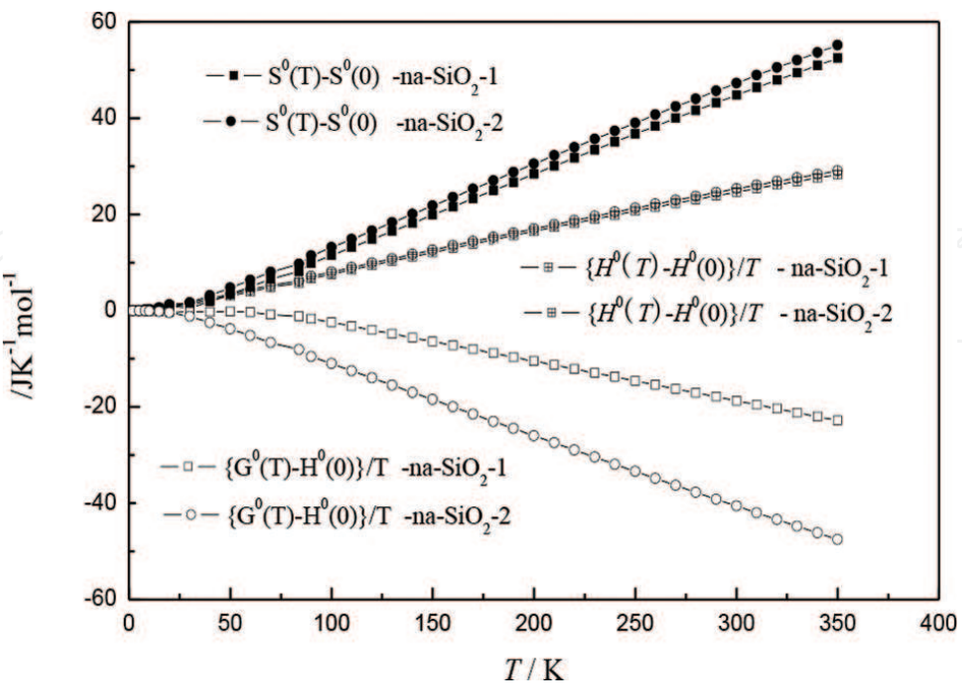


**Figure 12.** Entropy, enthalpy and Gibbs free energy of nano amorphous $SiO_2$ as functions of temperature.

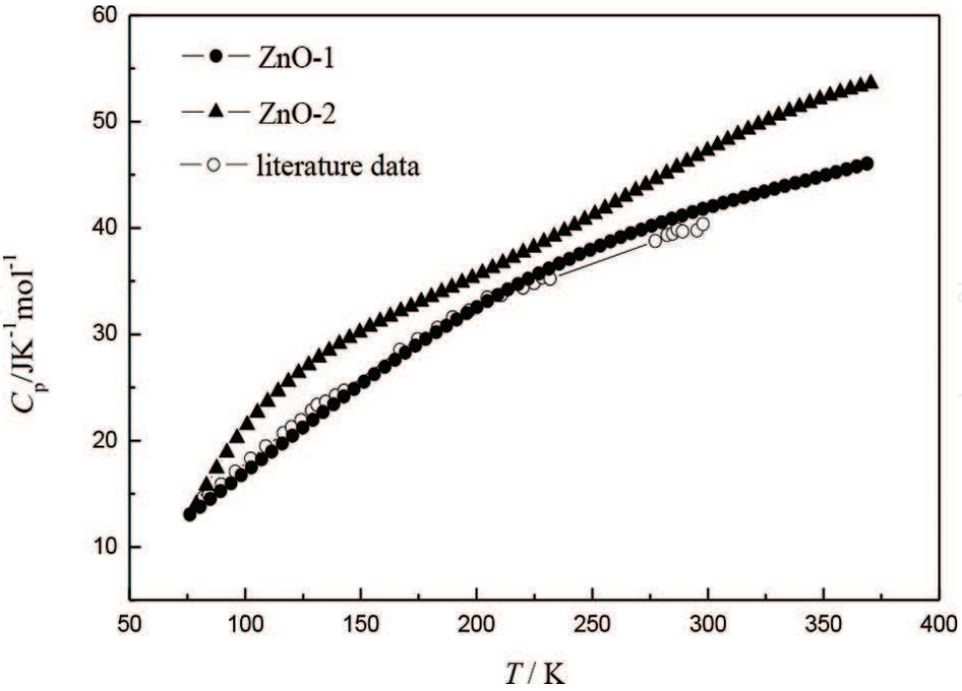


**Figure 13.** Heat capacity of nanocrystalline ZnO and the literature heat capacity data of coarse-grained crystalline ZnO.

should be introduced by vibrational and configurational entropy due to grain boundaries and lattice defects.

It seems to contradict our understanding of the above excess heat capacity, that nanocrystalline ZnO-1 and the more coarse-grained ZnO display very little difference. In fact, the grain size effect of nanocrystals on heat capacity has a size limit [50]. If the grain size is lower than the limit, the heat capacity will exhibit a great increase. Otherwise, heat capacity of nanocrystals and conventional polycrystals has little difference.

*3.2.2.4. Nanocrystalline $TiO_2$*

We measured heat capacity of nanocrystalline $TiO_2$ with three grain sizes by adiabatic calorimetry. $TiO_2$–2 and $TiO_2$–3 are anatase phase with the purity of 99% and $TiO_2$–1 is mainly anatase with a small amount of brookite phase. The experimental results were compared with reported heat capacity of coarse-grained anatase phase $TiO_2$ [51] in **Figure 14**. It is very obvious that the heat capacity of nanocrystalline was enhanced, and the heat capacities increase with grain size decreasing. The heat capacity enhancement of $TiO_2$–1 and $TiO_2$–2 was plotted in **Figure 14**. In the temperature range from 100 to 300 K, the heat capacity enhancement of $TiO_2$–1 and $TiO_2$–2 were 7–13% and 4–7%, respectively. The heat capacity enhancement of $TiO_2$–1 relative to $TiO_2$–2 was 3–6%, while the enhancement of $TiO_2$–2 relative to $TiO_2$–3 was only about 1%. Considered the size decreasing step is equal from $TiO_2$–3 to $TiO_2$–2 and from $TiO_2$–2 to $TiO_2$–1, the nanocrystalline size is not the main factor affected the heat capacity enhancement in this case. The sample of $TiO_2$–1 contains mainly anatase phase with a small amount of brookite phase and the samples of $TiO_2$–2 and $TiO_2$–3 are all anatase phase, so we can draw a conclusion that the small amount of heteromorphic

http://dx.doi.org/10.5772/intechopen.76151

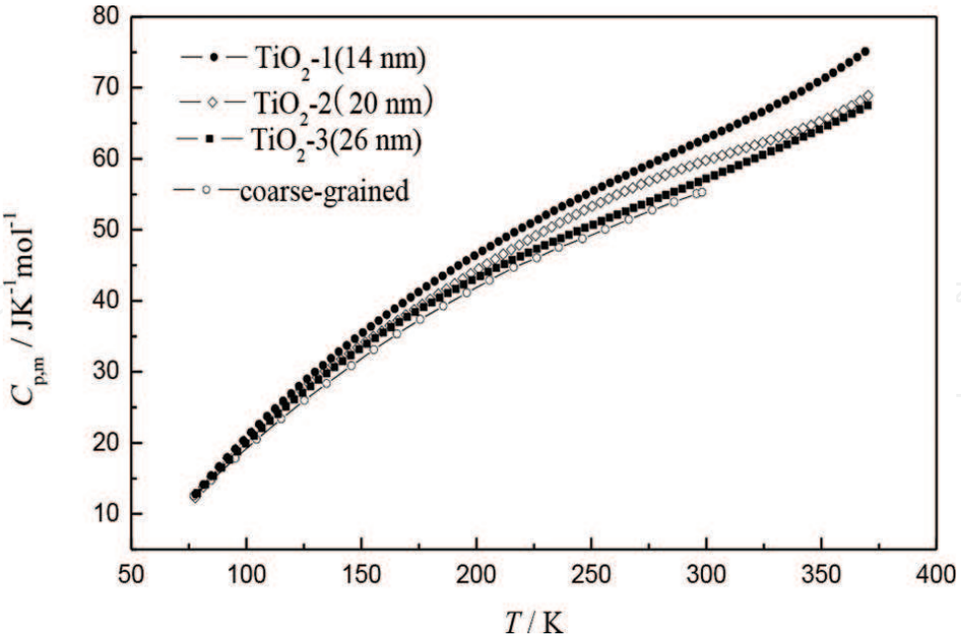


**Figure 14.** Heat capacity of anatase phase nanocrystalline $TiO_2$ with different grain sizes.

impurity makes more contribution to the heat capacity enhancement than the grain size. Recently research work by Boerio-Goats et al. reported that the water or other solvents absorbed on nanoparticle surfaces lead to heat capacity enhancement of anatase phase nanopartiles [52] (**Figures 15–17**).

*3.2.2.5. Nanocrystalline $ZrO_2$*

Nanocrystalline $ZrO_2$ with grain size of 18 nm was measured by adiabatic heat capacity calorimetry and compared with literature data of coarse-grained $ZrO_2$ [53]. The sample was prepared with the method of azeotropic distillation, and the purity is more than 99%. The heat capacity enhancement of nanocrystalline $ZrO_2$ was much larger than those of above nanostructured oxides. The enhancement was about 2–21% in the temperature range from 100 to 300 K, and exhibited a rising tendency with the temperature increasing. Many researchers theoretically explained the excess heat capacity of nano materials by excess volume, and some theoretical calculations have indicated that heat capacity enhancement sharply increases with the excess volume increasing when temperature rises [54]. We measured the density of the nanocrystalline $ZrO_2$ sample (5.2 g·cm$^3$) to be 93% of the coarse-grained $ZrO_2$ (5.6 g·cm$^3$). This difference in density is not very obvious and can hardly lead to 2–21% of heat capacity enhancement. We also measured the chemical purity of the nanocrystalline $ZrO_2$ to be 98.4%, so the contribution of impurity contained in the nanocrystalline to heat capacity enhancement cannot be neglected. We presume that heat capacity enhancement in the nanocrystalline $ZrO_2$ is mainly caused by impurity contained in it. Impurity in nano materials is not the general case of adulteration, since it is not avoided in the process of sample preparation, but it can bring activity to the materials. So nanocrystalline $ZrO_2$ has higher activity than coarse-grained one and is mostly used as a catalyst in some reactions.

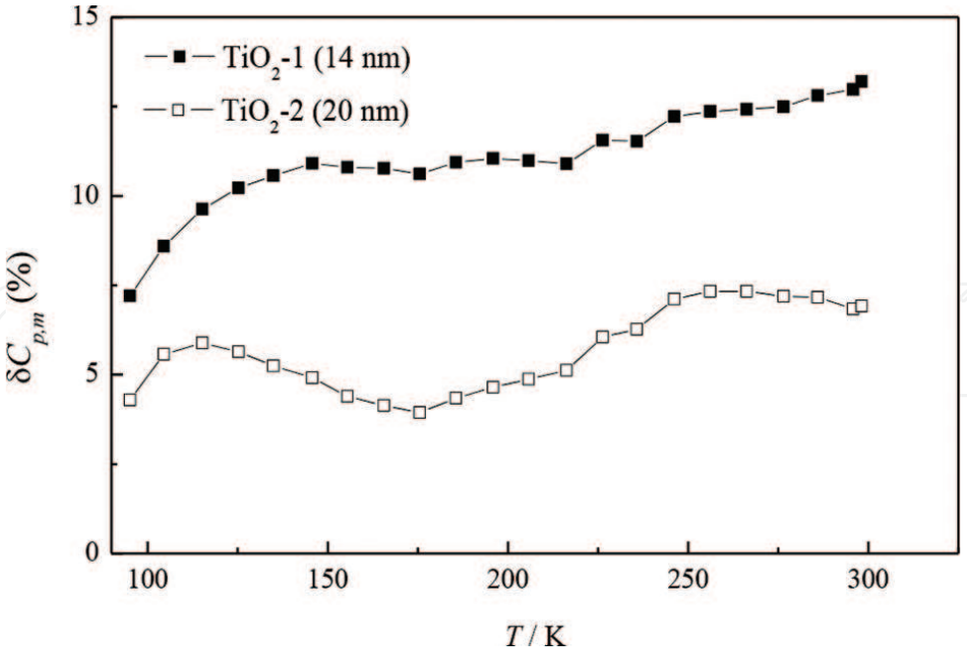


**Figure 15.** Heat capacity enhancement of nanocrystalline $TiO_2$ as a function of temperature, $\delta C_{p,m}$ (%) = 100%*[$C_{p,m(nano)}$ – $C_{p,m(coarse)}$]/$C_{p,m(coarse)}$.

### *3.2.3. Nanocrystalline metal*

Nanocrystalline metals are studied mostly in theory because its molecular structure is simple and easily calculated and explained. Those materials differ from glasses and crystals in the sense that they exhibit little short-range or long-range order. A series of novel physical

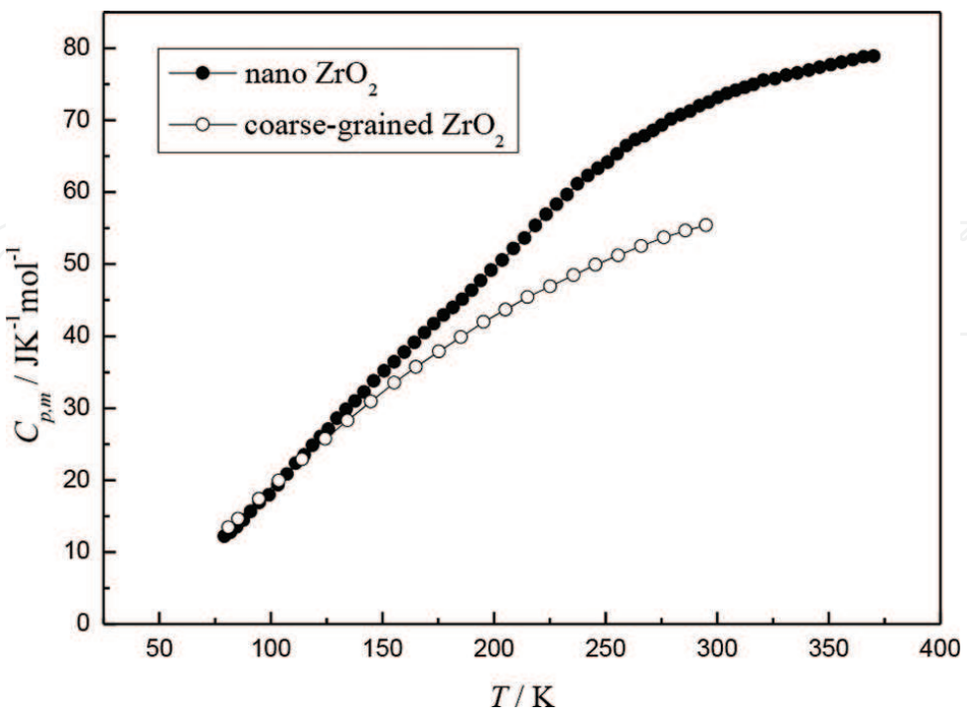


**Figure 16.** Heat capacity of nanocrystalline $ZrO_2$ and the literature heat capacity data of coarse-grained crystalline $ZrO_2$.

http://dx.doi.org/10.5772/intechopen.76151

and chemical properties of the nanocrystals, such as high diffusivity and reactivity, great ductility, large thermal expansion, enhanced phonon specific heat, and a significant change in the magnetic susceptibility, relative to the corresponding coarse-grained polycrystals, have captured the attention of the scientists and engineers because of their potential application. We measured heat capacities of nanocrystalline nickel and copper in the temperature range from 78 K to 370 K, and studied the heat capacity enhancement relative to the corresponding coarse-grained metal crystal. The two samples were produced by Zhengyuan Nano-materials Engineering Corp. (Shandong, China). The labeled chemical purity is not less than 99%.

*3.2.3.1. Nanocrystalline nickel*

Heat capacity of 40 nm nanocrystalline nickel was plotted in **Figure 17** and compared with the literature data [55] of coarse-grained crystalline nickel. From insert in the figure we can see that heat capacity enhancement varies between 2 and 4% in the temperature range from 100 to 370 K. The heat capacity enhancement in nanocrystalline materials are usually associated with an increase in the configurational and vibrational entropy of the grain boundaries, which constitute a large volume fraction of the material. The atomic fraction of the grain-boundary component can be approximately estimated to be 3δ/d, where d is the average size of crystalline grain and δ is the average thickness of interfaces which is known to be on the order of three or four atomic layers. For the nanocrystalline nickel with d = 40 nm, about 10% atoms are on the grain boundaries. Thus, the grain-boundary configurations or the grain-boundary energy should be responsible for the heat capacity enhancement.

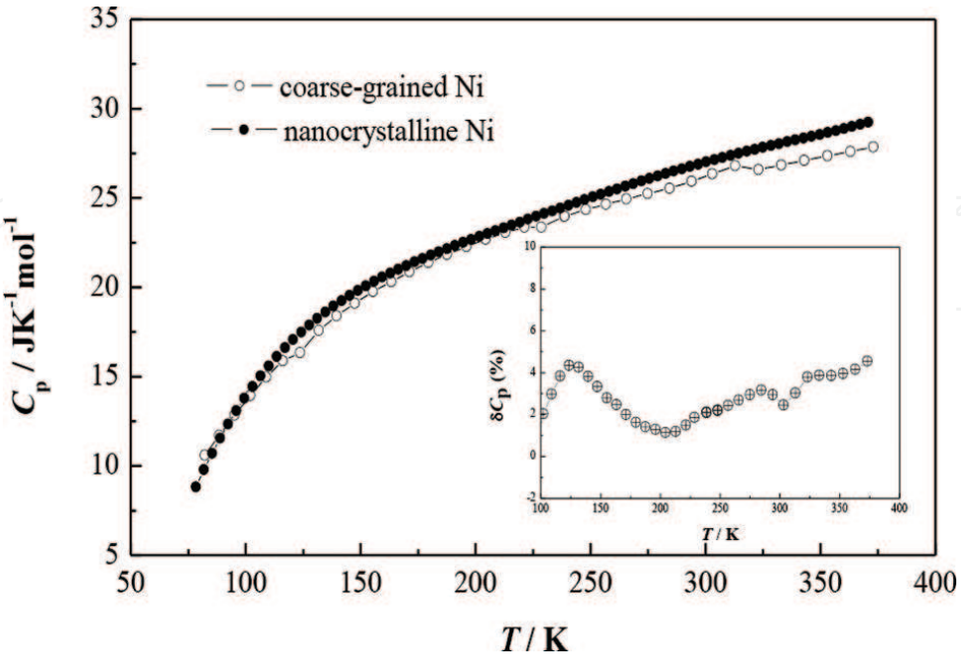


**Figure 17.** Heat capacity of nanocrystalline nickel and the literature heat capacity data of coarse-grained crystalline nickel, insert is heat capacity enhancement of nanocrystalline nickel.

*3.2.3.2. Nanocrystalline copper*

**Figure 18** shows the heat capacity of 50 nm nanocrystalline copper and the literature data [56] of coarse-grained one. The heat capacity enhancement is about 3–6% in the temperature range from 100 to 370 K. The purity of nanocrystalline copper is more than 99%, so the contribution of impurity to the enhancement is almost negligible. The relative density of nanocrystalline copper to the coarse-grained is 51% indicating a more open atomic structure of the grain-boundary component than coarse-grained polycrystalline copper, so the interatomic coupling becomes weaker and enhances heat capacity. In the theoretical calculation by Fecht et al., [57], thermal expansion coefficient is related to heat capacity, and the larger thermal expansion coefficient becomes, the more heat capacity enhances. We measured thermal expansion coefficient of nanocrystalline copper ($3 \times 10^{-5}$ $K^{-1}$) to be about two times of the coarse-grained copper's ($1.6 \times 10^{-5}$ $K^{-1}$). Thus, we can also explain the heat capacity enhancement of nanocrystalline copper with the increasing thermal expansion coefficient.

*3.2.4. Nanosized and microsized zeolite*

Nanosized zeolite is only different from microsized zeolite in the size, but its properties have varied much in some aspects when it changes into microsized zeolite. We carried out adiabatic heat capacity measurement on nanoszied and microsized ZMS-5, and compared their thermodynamic properties. From **Figure 19** it can be clearly seen that the heat capacities of nanosized ZMS-5 are larger than the microsized one. The heat capacity enhancement in the low temperature is not very obvious, but becomes larger with the temperature increasing.

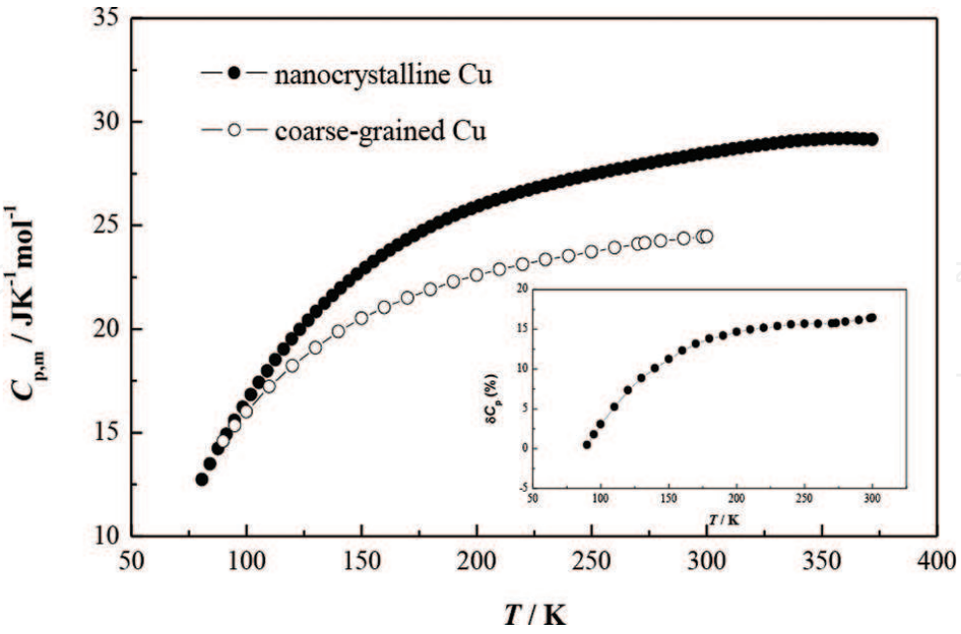


**Figure 18.** Heat capacity of nanocrystalline copper and the literature heat capacity data of coarse-grained crystalline copper, insert is heat capacity enhancement of nanocrystalline copper.

http://dx.doi.org/10.5772/intechopen.76151

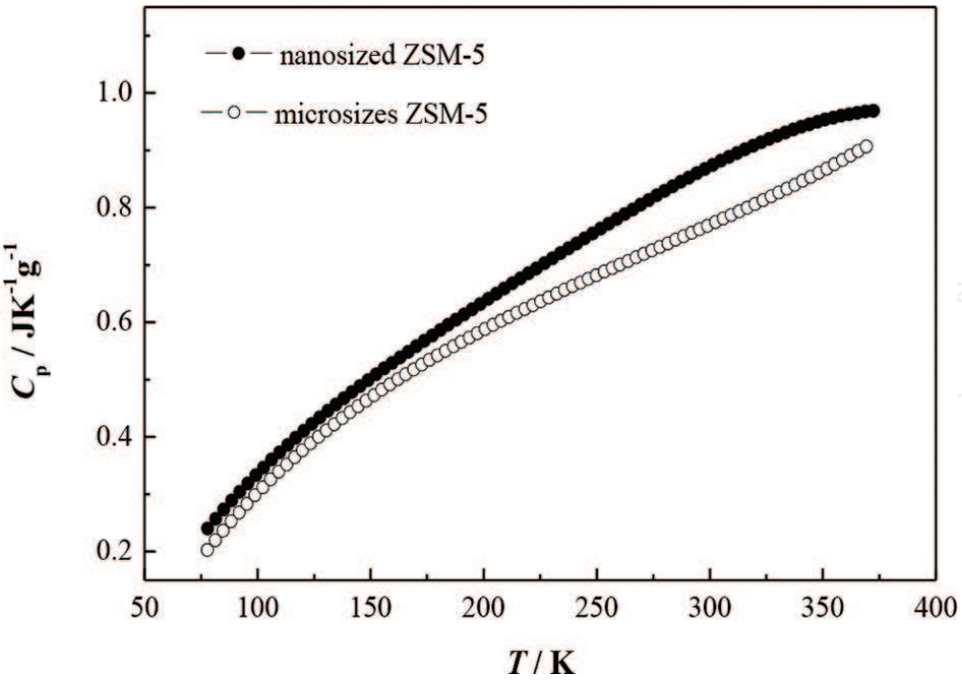


**Figure 19.** Heat capacity of nanosized and microsized ZSM-5.

Nanosized ZMS-5 possesses excess specific surface and behaves more activity than the microsized. This excess specific surface supplies more surface energy for nanosized ZMS-5 and enhances heat capacity.

## 4. Conclusions

A fully automated high-precision adiabatic calorimeter used for heat capacity measurement in the temperature range of 80–400 K was constructed. The reliability of the calorimeter was verified by measuring the heat capacities of synthetic sapphire ($\alpha$-$Al_2O_3$), Standard Reference Material 720. The deviation of the data obtained by this calorimeter from those published by NIST was within ±0.1% in the temperature range from 80 to 400 K. The adiabatic calorimeter can be used for precise measurement of molar heat capacities of condensed materials with important scientific value.

The heat capacities of IL [EMIM][TCB] were measured over the temperature range from 78 to 370 K by the high-precision-automated adiabatic calorimeter. Based on the heat capacity measurement experiments, the thermodynamic properties of fusion were calculated, and the thermodynamic functions $[H_T^0 - H_{298.15}^0]$ and $[S_T^0 - S_{298.15}^0]$ were derived in the range from 78 to 370 K with temperature interval of 5 K. The melting temperature, standard molar enthalpy and entropy of fusion were determined to be (283.123 ± 0.025) K, (12.973 ± 0.008) kJ·mol$^{-1}$ and (45.821 ± 028) J·K$^{-1}$·mol$^{-1}$, respectively. The IL was shown to be thermostable below 570 K and began to lose weight at 592.83 K.

Five kinds of nanostructured oxide materials, $Al_2O_3$, $SiO_2$, $TiO_2$, $ZnO_2$, $ZrO_2$, and two kinds of nanocrystalline metals: nickel and copper were investigated from heat capacity measurements. It is found that heat capacity enhancement in nanostructured materials is influenced by many factors, such as density, thermal expansion, sample purity, surface absorption, size effect, and so on. But the dominant factor affected heat capacity enhancement is different in different nanostructured materials. Only with careful and entire investigation on the particular properties of nanostructured materials, we can discuss and analyze the heat capacity enhancement. On the other hand, adiabatic calorimetry is the most direct method to measure heat capacity enhancement in nanostructured materials, however in order to set up thermodynamic theoretical model to describe and understand heat capacity enhancement, more theoretical calculation study and other experimental measurements should be further carried out.

## Acknowledgements

This work was financially supported by the National Natural Science Foundation of China under the grant NSFC No.21473198 and No. 20073047. Some parts of this chapter are reproduced from authors' recent conference publication, work, etc.

## Author details

Zhi Cheng Tan*, Quan Shi and Xin Liu

*Address all correspondence to: tzc@dicp.ac.cn

Thermochemistry Laboratory, Dalian Institute of Chemical Physics, Chinese Academy of Science, Dalian, China

## References

[1] Tan ZC, Di YY. Review of modern low temperature adiabatic calorimetry. Progress in Chemistry. 2006;**18**:1234

[2] Lang BE, Boerio-Goates J, Woodfield BF. Design and construction of an adiabatic calorimeter for samples of less than 1 cm3 in the temperature range $T$ = 15 K to $T$ = 350 K. The Journal of Chemical Thermodynamics. 2006;**38**:1655

[3] Kobashi K, Kyomen T, Oguni M. Construction of an adiabatic calorimeter in the temperature range between 13 and 505 K, and thermodynamic study of 1-chloroadamantane. Journal of Physics and Chemistry of Solids. 1998;**59**:667

[4] Sorai M, Kaji K, Kaneko Y. An automated adiabatic calorimeter for the temperature-range 13 K to 530 K the heat-capacities of benzoic-acid from 15 K to 305 K and of synthetic sapphire from 60 K to 505 K. The Journal of Chemical Thermodynamics. 1992;**24**:167

[5] Matsuo T, Suga H. Adiabatic microcalorimeters for heat-capacity measurement at low-temperature. Thermochimica Acta. 1985;**88**:149

[6] Inaba A. An adiabatic calorimeter for use at intermediate and higher temperatures - the heat-capacity of synthetic sapphire (alpha-$Al_2O_3$) from 70 K to 700 K. Journal of ChemicalThermodynamics. 1983;**15**:1137

[7] Ditmars DA, Ishira S, Chang SS, Bernstein G, West ED. Enthalpy and heat-capacity standard reference material - synthetic sapphire (alpha-$Al_2O_3$) from 10 to 2250 K. Journal of Research of the National Bureau of Standards. 1982;**87**:159

[8] Andrews JTS, Norton PA, Westrum EF Jr. Adiabatic calorimeter for use at super-ambient temperatures - heat-capacity of synthetic sapphire (alpha-$Al_2O_3$) from 300K to 550K. The Journal of Chemical Thermodynamics. 1978;**10**:949

[9] Westrum EF Jr, Furukawa GT, McCullough JP. In: McCullough JP, Scott DW, editors. Experimental Thermodynamics, Vol. I Calorimetry of Non-reacting Systems. London: Butterworths; 1968. p. 133

[10] Tan ZC, Li FX. An automatic adiabatic calorimeter for heat capacity measurements of solids in the range 4.2-30 K. Thermochimica Acta. 1995:253,189

[11] Tan ZC, Yin AX, Cheng SX, Zhou LX. An automated adiabatic calorimeter for heat capacity measurements between 20 and 90 K. Thermochimica Acta. 1988:123,105

[12] Tan ZC, Yin AX, Cheng SX, Zhou LX. National Standard of heat capacity measurement of solids in the range of 4.2 - 90 K. Science in China, Series B. 1991;**34**:560

[13] Tan ZC, Zhou LX, Cheng SX, Yin AX, Sun Y, Ye JC, Wang X. An adiabatic calorimeter for heat capacity measurements from 80 to 400 K —Heat capacities of alpha-alumina and *n*-heptane. Scientia Sinica, Series B. 1983;**26**:1014

[14] Yin AX, Wang WB, Tan ZC. Construction of microcomputer control measurements of low temperature heat capacity. Computers and Applied Chemistry. 1990;**7**:176

[15] Tan ZC, Liu BP, Yan JB, Sun LX. Computers and Applied Chemistry. 2003;**20**:264

[16] Tan ZC, Sun GY, Sun Y. An adiabatic low-temperature calorimeter for heat capacity measurement of small samples. Journal of Thermal Analysis. 1995;**45**:59

[17] Tan ZC, Sun GY, Song YJ, Wang L, Han JR, Liu YS, Wang M, Nie DZ. An adiabatic calorimeter for heat capacity measurements of small samples, the heat capacity of nonlinear optical materials $KTiOPO_4$ and $RbTiOAsO_4$ crystals. Thermochimica Acta. 2000;**247**:352

[18] Tan ZC, Zhang JB, Meng SH, Li L. A small sample-size automated adibadic calorimeter from 70 to 580 K-Molar heat capacities of alpha—$Al_2O_3$. Science in China, Series B. 1999;**42**:382

[19] Tan ZC, Sun LX, Meng SH, Li L, Xu F, Yu P, Liu BP, Zhang JB. Heat capacities and thermodynamic functions of P-chlorobenzoic acid. The Journal of Chemical Thermodynamics. 2002;**34**:1417

[20] Tan ZC, Ye JC, Sun Y, Cheng SX, Zhou LX. An adiabatic calorimeter for heat capacity measurements in the temperature range 300-600 K and pressure range 0.1-15 MPa. Thermochimica Acta. 1991;**183**:29

[21] Tan ZC, Shi Q, Liu BP, Zhang HT. A fully automated adiabatic calorimeter for heat capacity measurement between 80 and 400 K. Journal of Thermal Analysis and Calorimetry. 2008;**92**:367

[22] Sun Y, Tan ZC, Yin AX. An automated adiabatic copper block calorimeter for enthalpy measurements in the range of 400-1700 K. Acta Metrologica Sinica. 1982;**3**:301

[23] AGILENT, HP. 34970A Data Acquisition/Switch Unit, User'S Guide. 2nd ed. Hewlett Packard; 1997

[24] AGILENT, HP. 34420A Nano Volt/Micro-Ohm Meter, User's Guide. 2nd ed. Hewlett Packard; 2003

[25] Archer DG. Thermodynamic properties of synthetic sapphire (alpha—$Al_2O_3$), standard reference material 720 and the effect of temperature-scale differences on thermodynamic properties. Journal of Physical and Chemical Reference Data. 1993;**22**:1411

[26] Heintz A. Recent developments in thermodynamics and thermophysics of non-aqueous mixtures containing ionic liquids. A review. The Journal of Chemical Thermodynamics. 2005;**37**:525

[27] Ikegami S, Hamamoto H. Novel Recycling System for Organic Synthesis via Designer Polymer-Gel Catalysts. Chemical Reviews. 2009:109,583

[28] Rogers RD, Seddon KR, editors. Ionic Liquids: Industrial Application for Green Chemistry, ACS Symposium Series 818. Washington DC: American Chemical Society; 2002

[29] Rogers RD, Seddon KR, editors. Ionic Liquids as Green Solvents: Progress and Prospects, ACS Symposium Series 856. Washington DC: American Chemical Society; 2003

[30] Gurkan BE, de la Fuente JC, Mindrup EM, Ficke LE, Goodrich BF, Price EA, Schneider WF, Brennecke JF. Equimolar $CO_2$ Absorption by Anion-Functionalized Ionic Liquids. Journal of the American Chemical Society. 2010;132:2116

[31] Wang SF, Chen T, Zhang ZL, Pang DW, Wong KY. Effects of hydrophilic room-temperature ionic liquid 1-butyl-3-methylimidazolium tetrafluoroborate on direct electrochemistry and bioelectrocatalysis of heme proteins entrapped in agarose hydrogel films. Electrochemistry Communications. 2007;**9**:1709

[32] Gordon CM. New developments in catalysis using ionic liquids. Applied Catalysis A-General. 2001;**222**:101

[33] Olivier-Bourbigou H, Magna L, Morvan D. Ionic liquids and catalysis: Recent progress from knowledge to applications. Applied Catalysis A-General. 2010;**373**:1-56

[34] Yan PF, Yang M, Liu XM, Wang C, Tan ZC, Welz-Biermann U. Activity coefficients at infinite dilution of organic solutes in the ionic liquid 1-ethyl-3-methylimidazolium etracyanoborate [EMIM][TCB] using gas–liquid chromatography. The Journal of Chemical Thermodynamics. 2010;**42**:817

[35] Verevkin SP, Vasiltsova TV. Bich E, Heintz A. Thermodynamic properties of mixtures containing ionic liquids. Activity coefficients of aldehydes and ketones in 1-methyl-3-ethyl-imidazolium bis(trifluoromethyl-sulfonyl) imide using the transpiration method. Fluid Phase Equilibria. 2004;**218**:165

[36] Heintz A, Kulikov DV, Verevkin SP. Thermodynamic properties of mixtures containing ionic liquids. Activity coefficients at infinite dilution of polar solutes in 4-methyl-N-butyl-pyridinium tetrafluoroborate using gas-liquid chromatography. Journal of Chemical Thermodynamics. 2002:341,1347

[37] Yang JZ, Jin Y, Xu WG, Zhang QG, Zang SL. Studies on mixture of ionic liquid EMIGa$Cl_{14}$ and EMIC. Fluid Phase Equilibria. 2005;**227**:41

[38] Tong B, Liu QS, Tan ZC, Welz-Biermann U. Thermochemistry of Alkyl Pyridinium Bromide Ionic Liquids: Calorimetric Measurements and Calculations. The Journal of Physical Chemistry. A. 2010;**114**:3782

[39] Verevkin SP, Emel'yanenko VN, Toktonov AV, Goodrich P, Hardacre C. Thermochemistry of Ionic Liquid Catalyzed Reactions. Experimental and theoretical study of chemical equilibria of izomerization and transalkylation of tert-amylbenzenes. The Journal of Physical Chemistry. B. 2009;**113**:12704

[40] Verevkin SP, Emel'yanenko VN, Toktonov AV, Leolko AS, Duwensee J, Kragl U, Sarge SM. Thermochemical and Ab initio studies of biodiesel fuel surrogates: 1,2,3-propanetriol triacetate, 1,2-ethanediol diacetate, and 1,2-ethanediol monoacetate. Industrial and Engineering Chemistry Research. 2009;**48**:7388

[41] Gomes de Azevedo R, Esperança JMSS, Szydlowski J, Visak ZP, Pires PF, Guedes HJR, Rebelo LPN. Thermophysical and thermodynamic properties of ionic liquids over an extended pressure range:bmim $NTf_2$ and hmim $NTf_2$. Journal of Chemical Thermodynamics. 2005;**37**:888

[42] Bernhardt E, Finze M, Willner H. An efficient synthesis for tetracyanoborates by sinter processes. Zeitschrift für anorganische und allgemeine Chemie. 2003;**629**:1229

[43] Ignat'ev NV, Welz-Biermann U, Kucheryna A, Bissky G, Willner H. New ionic liquids with tris(perfluoroalkyl)trifluorophosphate (FAP) anions. Journal of Fluorine Chemistry. 2005;**126**:1150

[44] Tong B, Tan ZC, Meng CG, Cui LJ, Xiao G, Liu RB. Thermodynamic investigation of several natural polyols (IV): Heat capacities and thermodynamic properties of adonitol. Thermochimica Acta. 2010;**499**:117

[45] Tong B, Tan ZC, Wang SX. Low Temperature Heat Capacities and Thermodynamic Properties of 2-Methyl-2-butanol. Chinese Journal of Chemistry. 2008;**26**:1561

[46] Rupp J, Birringer R. Enhanced specific-heat-capacity (*Cp*) measurements (150-300 K) of nanometer-sized crystalline materials. Physics Review. 1987;**B 36**:7888

[47] Wang L. Ph.D. Thesis. Thermochemistry study of nanostructured materials, supervised by Prof.Tan ZC. Dalian, China: Dalian Institute of Chemical Physics, Chinese Academy of Sciences; 2001

[48] Wang L, Tan ZC, Meng SH, Liang DB, Li GH. Enhancement of molar heat capacity of nanostructured $Al_2O_3$ Nanoparticle. Journal of Nanoparticle Research. 2001;**3**:483

[49] Millar RW. The heat capacity at low temperatures of zinc oxide and of cadmium oxide. Journal of the American Chemical Society. 1928;**50**:2653

[50] Tschöpe A, Birringer R. Thermodynamics of nanocrystalline platinum. Acta Metallurgica Materialia. 1993;**41**:2791

[51] Shimate CH. Heat capacities at low temperatures of titanium dioxide (rutile and anatase). Journal of the American Chemical Society. 1947;**69**:218

[52] Boerio-Goates J, Li G, Li L, Walker TF, Parry T, Woodfield BF. Surface water and the origin of the positive excess specific heat for 7 nm rutile and anatase nanoparticles. Nano Letters. 2006;**6**(4):750

[53] Kelley KK. Specific heat of $ZrO_2$ at low temperatures. Industrial and Engineering Chemistry. 1944;**36**:377

[54] Wagner M. Structure and thermodynamic properties of nanocrystalline metals. Physics Review, B. 1992;**45**:635

[55] Busey RH, Giauque WF. The heat capacity of nickel from 15 to 300 K - entropy and free energy functions. Journal of the American Chemical Society. 1952;**74**:3157

[56] Martin DL. Tray type calorimeter for the 15-300 K temperature-range - copper as a specific-heat standard in this range. The Review of Scientific Instruments. 1987;**58**:639

[57] Fecht HJ. Thermodynamics of nano-grain boundaries. Materials Research Society Symposia Proceedings. 1991;**206**:587